HHS Public Access

Author manuscript

Cell Rep. Author manuscript; available in PMC 2021 December 03.

Published in final edited form as:

Cell Rep. 2021 August 24; 36(8): 109594. doi:10.1016/j.celrep.2021.109594.

Modulation of motor behavior by the mesencephalic locomotor region

Daniel Dautan[1,*], **Adrienn Kovács**[2], **Tsogbadrakh Bayasgalan**[2], **Miguel A. Diaz-Acevedo**[1], **Balazs Pal**[2], **Juan Mena-Segovia**[1,3,*]

[1]Center for Molecular and Behavioral Neuroscience, Rutgers University, Newark, NJ 07102, USA

[2]Department of Physiology, University of Debrecen, Faculty of Medicine, 4012 Debrecen, Hungary

[3]Lead contact

SUMMARY

The mesencephalic locomotor region (MLR) serves as an interface between higher-order motor systems and lower motor neurons. The excitatory module of the MLR is composed of the pedunculopontine nucleus (PPN) and the cuneiform nucleus (CnF), and their activation has been proposed to elicit different modalities of movement. However, how the differences in connectivity and physiological properties explain their contributions to motor activity is not well known. Here we report that CnF glutamatergic neurons are more electrophysiologically homogeneous than PPN neurons and have mostly short-range connectivity, whereas PPN glutamatergic neurons are heterogeneous and maintain long-range connections, most notably with the basal ganglia. Optogenetic activation of CnF neurons produces short-lasting muscle activation, driving involuntary motor activity. In contrast, PPN neuron activation produces long-lasting increases in muscle tone that reduce motor activity and disrupt gait. Our results highlight biophysical and functional attributes among MLR neurons that support their differential contribution to motor behavior.

In brief

Dautan et al. show key differences in the connectivity and physiological properties of neurons of the mesencephalic locomotor region. Although activation of CnF neurons elicits involuntary locomotor responses, activation of PPN neurons increases muscle tone and reduces motor activity, suggesting that PPN encodes a readiness signal that precedes locomotion.

*Correspondence: dautan.daniel@outlook.com (D.D.), juan.mena@rutgers.edu (J.M.-S.).

AUTHOR CONTRIBUTIONS

J.M.-S. and D.D. conceptualized the project. D.D., A.K., T.B., M.A.D.-A., and B.P. performed experiments. D.D., A.K., T.B., M.A.D.-A., and B.P. analyzed the data. D.D., M.A.D.-A., B.P., and J.M.-S. wrote the original draft. All authors contributed to reviewing and editing the final version of the manuscript. J.M.-S. supervised the project.

DECLARATION OF INTERESTS

The authors declare no competing interests.

SUPPLEMENTAL INFORMATION

Supplemental information can be found online at https://doi.org/10.1016/j.celrep.2021.109594.

Graphical Abstract

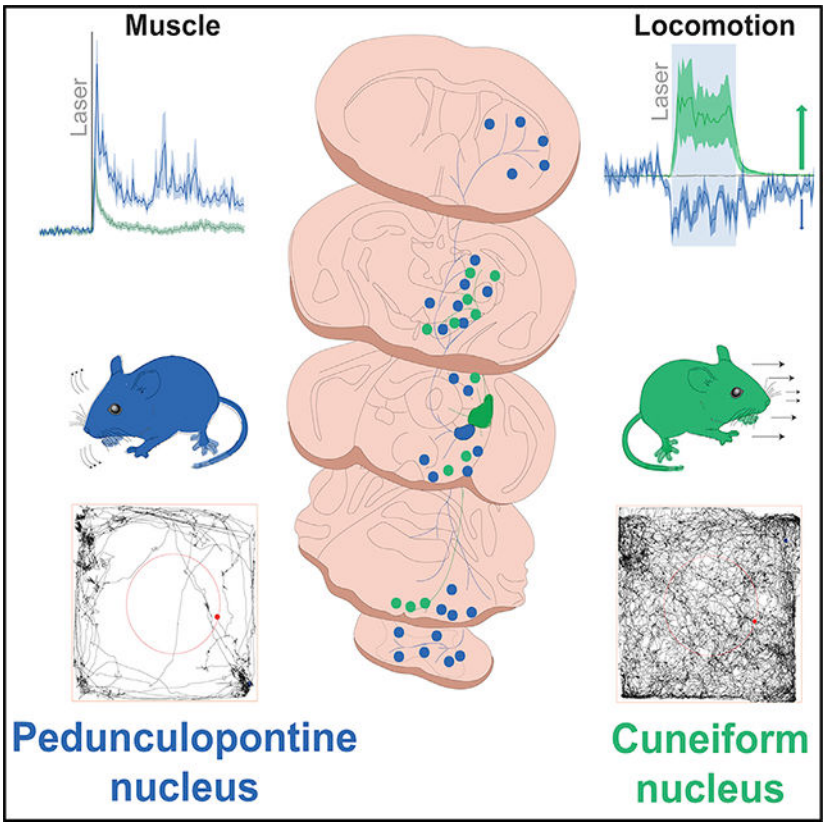

INTRODUCTION

The mesencephalic locomotor region (MLR) is a functionally defined midbrain area composed of the pedunculopontine nucleus (PPN) and the cuneiform nucleus (CnF), which has been typically described as an output station of forebrain systems reaching lower motor circuits (Capelli et al., 2017; Dautan et al., 2014, 2016a, 2016b; Galtieri et al., 2017; Garcia-Rill et al., 1983; Huerta-Ocampo et al., 2020; Kim et al., 2017; Mena-Segovia and Bolam, 2017). Early experiments defined the MLR by demonstrating that electrical stimulation of this region induced a locomotor response in decorticated cats (Garcia-Rill et al., 1987; Shik et al., 1966). More recently, optogenetic experiments revealed that the motor function of the MLR depends on excitatory transmission from glutamatergic neurons (Caggiano et al., 2018; Roseberry et al., 2016), which is the most prominent cell type in the MLR (Martinez-Gonzalez et al., 2012; Wang and Morales, 2009). In the last two decades, a role for these circuits in gait and posture has been proposed (Gatto and Goulding, 2018; Josset et al., 2018; Lau et al., 2015; Pahapill and Lozano, 2000). Moreover, degeneration of neurons in the MLR may underlie some motor impairments in Parkinson's disease (Hepp et al., 2013; Hirsch et al., 1987; Jellinger, 1988; Manaye et al., 1999; Zweig et al., 1987, 1989). Deep brain stimulation into the PPN has been shown to produce some improvements in abnormal gait based on the idea that the output from the MLR is excitatory (Goetz et al., 2019; Jenkinson et al., 2004; Nandi et al., 2002; Perera et al., 2018). However, it is not

fully understood how excitatory MLR neurons contribute to motor behavior and how motor functions are associated with different neuronal types in the MLR.

The PPN, the largest component of the MLR, is highly heterogeneous. It is composed of three neurotransmitter-defined cell types: cholinergic, γ-aminobutyric acid-ergic (GABAergic) and glutamatergic neurons. Among PPN glutamatergic neurons, a high degree of variability has been reported in their neurochemical composition (Martinez-Gonzalez et al., 2012), connectivity (Roš et al., 2010), and firing properties (Petzold et al., 2015). Comparatively less is known about the CnF. Reports show that activation of CnF glutamatergic neurons induces robust motor activation that is functionally distinct from the activation of PPN neurons, suggesting functional specialization of MLR neurons (Caggiano et al., 2018; Josset et al., 2018). PPN and CnF are contiguous structures, the borders of which are not well defined (Sherman et al., 2015), and this imposes a challenge for unambiguously separating both populations. Furthermore, there is a certain level of interconnectivity that accounts for an additional degree of difficulty in the interpretation of functional studies. Therefore, we sought to identify the functional properties of PPN and CnF neurons and their involvement in motor control.

We used a range of electrophysiological, behavioral, and anatomical techniques to dissect the properties of glutamatergic neurons in the PPN and CnF and identify their specific contributions to motor function and muscle activity. Our results establish fundamental differences in the properties and functions of the PPN and CnF.

RESULTS

Input/output connectivity of PPN and CnF with segregated motor circuits

To determine the afferent and efferent connectivity of MLR glutamatergic neurons, we used Cre-dependent anterograde and retrograde viral tracing strategies in VGLUT2-cre mice (Figure S1A). Given the proximity of MLR structures, only microinjections that were strictly confined to the borders of the PPN or the CnF were considered further (Figure S1B). We used the immune-labeling of choline acetyltransferase (ChAT) to delimit the boundaries of the PPN and the ventral border of the CnF (Mori et al., 1977; Nieuwenhuys and Puelles, 2016; Puelles, 2019; Sherman et al., 2015). CnF is bordered ventrally by the PPN and dorsally by the central nucleus of the inferior colliculus (cIC) and fibrodendritic lamina (Korte et al., 1992). A glutamatergic neuron was considered to belong to the PPN if it was located within 100 μm of the closest cholinergic neurons (Figure 1A) or to the CnF if it was located at least 100 μm dorsally to cholinergic neurons and ventral to the cIC (Figure 1B). If more than 5% of virus-labeled neurons were located outside the borders of the targeted structure, the data from the animal were excluded (Figure S1B).

To label the axonal projections and synapses originating in the PPN and CnF, we transduced glutamatergic neurons with a reporter expressing cytosolic green fluorescent protein (GFP) in the presence of Cre recombinase and a red fluorescent protein (mRuby) (Figure 1) under the control of the promoter for the pre-synaptic marker synaptophysin (AAV-hSyn-FLEX-GFP-2A-synaptophysin-mRuby) (PPN: n = 3, Figures 2A1 and 2A1′; CnF: n = 3, Figures 2A2 and 2A2′). We next mapped the synaptophysin expression across the brain and spinal

cord using high-resolution confocal imaging (Figures 2B and 2F). Only mRuby labeling that overlapped with yellow fluorescent protein (YFP) labeling was included in the quantification to reduce the inclusion of fluorescent artifacts (Figure 2F). No differences in the number of transduced neurons (GFP^+) between PPN and CnF were observed (Figure 2C). However, the overall density of synapses ($mRuby^+/GFP^+$ puncta) was higher in the PPN group compared with the CnF group (Figure 2D). We next compared the distribution of synapses across the brain between the groups (Figures 2B and 2E; see abbreviations in Table S1). We found comparatively more innervation by PPN than by CnF neurons in the basal ganglia (PPN: 0.336 ± 0.089 pixels/100 μm^2, CnF: 0.095 ± 0.032 pixels/100 μm^2; Wilcoxon rank-sum test, $p = 0.0369$; Figure 2F), as well as in individual structures such as the dorsal raphe (PPN: 0.56 ± 0.121 pixels/100 μm^2, CnF: 0.047 ± 0.023 pixels/100 μm^2; $p = 0.0292$) and the dorsal periaqueductal gray area (dPAG) (PPN: 0.251 ± 0.078 pixels/100 μm^2, CnF: 0.176 ± 0.034 pixels/100 μm^2; $p = 0.037$), in agreement with previous tracing studies (Assous et al., 2019; Futami et al., 1995; Lavoie and Parent, 1994). In contrast, the innervation originated in CnF glutamatergic neurons was mostly concentrated in the midbrain and similar to that of the PPN (PPN: 0.25 ± 0.028 pixels/100 μm^2, CnF: 0.17 ± 0.029 pixels/100 μm^2; $p = 0.0562$) and the pons (PPN: 0.14 ± 0.03 pixels/100 μm^2, CnF: 0.12 ± 0.033 pixels/100 μm^2; $p = 0.56$; Figure 2G), including the tectal area, the parabrachial nucleus, the periaqueductal gray area (PAG), and the ventral gigantocellular nucleus, in agreement with previous studies (Bajic and Proudfit, 2013; Geisler and Zahm, 2005; Mitchell et al., 1989). Furthermore, PPN neurons, but not CnF neurons, show synaptic labeling in the striatum, the substantia nigra pars compacta (4.27 ± 0.12 pixels/100 μm^2), the cerebellum (4.19 ± 0.04 pixels/100 μm^2), the dorsal brainstem (vestibular nucleus: PPN 0.77 ± 0.02 pixels/100 μm^2, CnF: 0 pixels/100 μm^2; medullary reticular nucleus [MdV]: PPN 0.4 ± 0.01 pixels/100 μm^2, CnF: 0 pixels/100 μm^2; Figure 2G), and the spinal cord (Figure 2J). PPN glutamatergic projections to the spinal cord were observed at all segments (Figure 2K), but the synaptic density was not quantified. Following axonal reconstructions of randomly selected cervical, thoracic, lumbar, and sacral segment sections (Figure 2K), we found that PPN projections follow the rubrospinal tract and decussate in laminae 5–7, making dense synapses (mRuby signal) that seem to avoid motor neurons (Figures 2J and 2K). Altogether, these findings suggest that the PPN directly projects to structures involved in different modalities of movement (i.e., basal ganglia, brainstem, cerebellum, and spinal cord), whereas the CnF sends projections to structures involved in the execution of movement (i.e., ventral gigantocellular nucleus) (Figure S2A).

Next, to identify the inputs to the glutamatergic neurons of the PPN and CnF, we used a monosynaptic retrograde labeling strategy in VGLUT2-cre mice (pseudotyped RvdG-YFP). Because the specificity of the retrograde tracing is conferred by the expression of the helper viruses, we adjusted the volume of the helper mix (AAV-DIO-TVA-mCherry, AAV-DIO-Rg, 1:1) to selectively target the PPN (Figure 3A; n = 3) or the CnF (Figure 3B; n = 3) according to the criteria described earlier (Figures 3A′–3B′). Animals with no overlap between helper viruses and RvdG did not produce labeling in input neurons (data not shown). Starter neurons (mCherry/YFP positive) within the PPN and CnF were located within the border of each structure (Figure 3C). The overall number of input neurons (YFP positive) was larger in the PPN group compared with the CnF group (Figure 3D). After normalization

by the number of starter neurons, the number of input neurons was still larger in the PPN group (PPN: 4.73 ± 1.27, CnF: 2.28 ± 0.94; p = 0.027). We found a larger number of input neurons to the CnF originating in the colliculi (PPN: 22 ± 1.74, CnF: 39.66 ± 8.46; Wilcoxon rank-sum test, p = 0.0033; Figure 3E), the PAG (PPN: 5.06 ± 0.44, CnF: 8.52 ± 0.92; p = 0.0275), and the precuneus (PPN: 7.46 ± 0.61, CnF: 15.238 ± 1.89; p = 0.0175), whereas a larger number of input neurons to the PPN originated in the PnO (PPN: 7.47 ± 0.21, CnF: 2.21 ± 1.46; p = 0.0234; Figure 3H), the striatum (PPN: 2.66 ± 1.55, CnF: 0.33 ± 1.15; p = 0.04; Figure 3I), the ZI (PPN: 4.33 ± 0.15, CnF: 1.18 ± 0.70; p = 0.025), and the motor cortex (PPN: 4.66 ± 0.66, CnF: 1.52 ± 1.52; p = 0.025; Figure 3J). Input neurons in a subset of motor structures were observed to connect exclusively with the PPN, including the SNr (PPN: 5.3 ± 0.39, CnF: 0; Figures 3F and 3G), spinal cord (PPN: 7.23 ± 0.96, CnF: 0; Figure 3K), gigantocellular nucleus (PPN: 0.98 ± 0.22, CnF: 0), dorsal gigantocellular nucleus (PPN: 2.16 ± 0.20, CnF: 0), paragigantocellular nucleus (PPN: 1.33 ± 0.13, CnF: 0), and deep cerebellar nuclei (PPN: 4.22 ± 0.55, CnF: 0; Figures 3E–3K; Figure S2B). Overall, the distribution of inputs to PPN glutamatergic neurons is far more widespread than the distribution of inputs to CnF glutamatergic neurons and largely overlaps with the PPN/CnF output targets (Figure 3L). In summary, and in agreement with a recent study reporting the input connectivity to PPN and CnF glutamatergic neurons (Caggiano et al., 2018), we found that the PPN receives larger input from the basal ganglia, pons, and medulla than the CnF, whereas the CnF receives larger input from the colliculi than the PPN; however, in contrast to Caggiano et al. (2018), our data show a more prominent cortical input to both PPN and CnF, as well as input neurons to the PPN in the spinal cord. Our results thus support differences in the input/output connectivity of PPN and CnF glutamatergic neurons with separate motor circuits (Figure S3).

Glutamatergic PPN neurons are physiologically distinct from CnF neurons

To characterize the physiological properties of MLR glutamatergic neurons, we obtained brain slices for *ex vivo* recordings of identified PPN (n = 77) and CnF (n = 41) glutamatergic neurons of VGLUT2-tdTomato mice (Figure 4; Figures S4A–S4L; Tables S2 and S3). From the recorded tdTomato-positive neurons, randomly selected subsets (PPN: n = 15, CnF: n = 11; Figures 4A and 4B) were subsequently labeled and reconstructed, revealing morphological differences between the two neuronal populations. The number of the dendrites of CnF glutamatergic neurons was significantly larger than in the PPN (5.11 ± 0.42 versus 3.66 ± 0.33; p = 0.007). Correspondingly, the number of endings was also significantly greater in the CnF than in the PPN (20 ± 4.56 versus 11.58 ± 1.73; p = 0.03). As expected, the number of nodes was greater in the CnF, although with borderline significance (15 ± 4.38 versus 8.08 ± 1.51; p = 0.05; Figures 4C and 4D; Table S2). Using the classical electrophysiological classification of PPN neurons (Kang and Kitai, 1990; Leonard and Llinás, 1994) (Figures S4A–S4L; Tables S2 and S3), we defined functional subgroups based on changes of spike frequency adaptation with increasing depolarization (Nigro et al., 2014) and classified neurons into 3 groups: non-adapting, slowly adapting, and rapidly adapting (Figures 4E–4G). In the PPN, 30.2% of all neurons (13/43 neurons) were non-adapting and were located predominantly in the lateral regions, whereas 21% (9/43 neurons) were slowly adapting and 48.8% (21/43 neurons) were rapidly adapting. In contrast, in the CnF, most neurons (85.7%, 24/28 neurons) were rapidly adapting, and non-

adapting and slowly adapting neurons constituted equal smaller proportions (7.15%, 2/28 neurons for each category) (Figure 4H). Thus, the responses of MLR glutamatergic neurons to spike adaptation reveal important biophysical group differences in the composition of the PPN and the CnF, ranging from firing frequency to adaptation index (Figures S4M and S4N; Table S2).

Next, because neurons in the MLR have been reported to display high-threshold membrane potential oscillations (Bordas et al., 2015; Takakusaki et al., 1997), we sought to characterize the oscillatory activity of glutamatergic neurons of the PPN and CnF. Oscillatory activity in the 10–20 Hz range was present in PPN glutamatergic neurons (n = 24 neurons) and was sensitive to tetrodotoxin (TTX) (Figure 4I). In contrast, oscillatory activity in the 20–40 Hz range was present in the CnF (n = 19 neurons), but it was weaker and largely insensitive to TTX (Figure 4J; Table S2). Furthermore, persistent sodium currents were observed predominantly in the PPN (9/11 neurons, range from 26 to 58.7 pA, average 32.5 ± 4.5 pA; Figure 4K) and to a lesser extent in the CnF (3/7 neurons, range from 7 to 22.2 pA, average 12.4 ± 4.9 pA; Figure 4L; Figures S4 and S5), suggesting the contribution of such currents to the oscillatory activity observed in PPN neurons. In summary, PPN glutamatergic neurons form a heterogeneous group and display robust, wide-range oscillatory activity and the presence of persistent sodium currents. In contrast, CnF glutamatergic neurons are largely fast adapting and mostly lack persistent sodium currents.

PPN and CnF activation produces contrasting effects on motor activity

The differences in the connectivity and physiological properties between PPN and CnF reported here suggest that neurons in each structure are recruited by different motor circuits and that their dynamics of activation differ. Recent reports have shown that CnF neurons modulate speed locomotion (Roseberry et al., 2016; Josset et al., 2018; Lee et al., 2014), whereas PPN neurons have been suggested to modulate exploratory locomotion (Caggiano et al., 2018) and locomotion pattern (Josset et al., 2018). To elucidate the extent of overlap of PPN and CnF function in the context of motor behavior, we used an optogenetic strategy to stimulate glutamatergic neurons while mice were tested in a battery of motor tasks (Figure 5). We unilaterally transduced ChR2 into the PPN or the CnF of VGLUT2-cre mice and implanted an optic fiber to deliver blue light and activate ChR2 (Figure S1B). Mice received stimulation at various frequencies (1, 10, and 20 Hz; 20-ms pulses) for 1 s, with an inter-stimulation interval of 9 s (laser off). First, we determined the effects in the open field (40 × 40 cm) (Figure 5A). Stimulation of CnF (n = 6 mice), but not PPN (n = 8 mice), increased motor activity compared with controls (CTRL: n = 8 mice) (Figures 5B–5H). The analysis of the stimulation effects on individual trials (i.e., trial-by-trial average aligned to the laser onset) revealed that stimulation of CnF glutamatergic neurons robustly increased the distance traveled compared with the baseline (Figure 5B). In contrast, stimulation of PPN glutamatergic neurons (Figure 5C) significantly reduced the distance traveled. To determine whether the stimulation effects depended on the behavioral state of the animal, we separated the stimulation trials based on whether animals were moving or not. We found that CnF stimulation increases the cumulative distance traveled and speed regardless of the behavioral state of the animal (Figure 5D), whereas PPN effects were only visible during ongoing movement (Figure 5E). Because the effects of PPN stimulation

reported here contrast with previous studies that reported an increase in motor activity during PPN activation (Caggiano et al., 2018; Roseberry et al., 2016), we next explored whether different stimulation protocols may account for the differences between studies. We used three stimulation frequencies (1, 10, and 20 Hz; 1 s on/9 s off; Figures 5F and 5G) and found that in line with the effects reported earlier, the cumulative effect of PPN stimulation over the entire 30 min session was consistently inhibitory, whereas the increase in motor activity elicited by CnF stimulation was frequency dependent (Figures 5F and 5G). In contrast, optogenetic inhibition of PPN glutamatergic neurons in the open field revealed a small, non-significant increase in distance traveled (Figures S6A and S6B). No differences in the time spent in the center versus the periphery of the open field were detected (Figure 5H), thus ruling out an anxiogenic effect of the stimulation. To further characterize the frequency-dependent effects reported earlier, we tested a different cohort of CnF-transduced and CnF-implanted animals (n = 6) in a larger open field (80 × 80 cm) with randomized stimulation frequencies ranging from 0.1 to 30 Hz (1 s on/9 s off). We found that all stimulation frequencies increased the distance traveled (Figure S7A), with a maximum effect observed at 12.5 Hz, and that the effect was restricted to the duration of the stimulation (Figure S7B; Video S1). These results reveal that CnF stimulation increases the distance traveled by generating robust and consistent bouts of motor activity, whereas stimulation of PPN neurons briefly reduces exploratory locomotion.

To determine whether the reduction in motor activity observed following PPN stimulation was the consequence of altering the behavioral state during exploratory locomotion (i.e., as evaluated earlier in the open field) or rather a pure motor effect, we next tested the mice during forced locomotion (custom-made motorized treadmill, 3 m/min constant speed), in which animals keep up walking at the front of the treadmill (as seen in controls; Figures 5I–5L). In the PPN group, blue light stimulation caused the mice to stop locomotion and lag at the rear of the treadmill (Figures 5J–5L). As expected, mice in the CnF group spent most of the time at the front of the treadmill and had a significantly larger traveled distance than those in the control and PPN groups (Figures 5I–5L). These results suggest that activation of PPN glutamatergic neurons reduces locomotion by decreasing overall motor activity.

Because the MLR, and specifically the PPN, have been proposed to have a key role in gait and balance, we next tested the mice in the elevated grid walk test, which evaluates skilled, coordinated movements requiring sensorimotor integration (Chao et al., 2012). Mice were placed on a 20 × 40 cm elevated grid (grid size of 1.5 cm) and allowed to explore freely for 20 min (Figures 6A and 6B). Compared with controls, stimulation of PPN neurons produced a significant reduction in the distance traveled, distance to the center of the grid, and movement speed (PPN: n = 6, control: n = 11; Figures 6B–6D; Figure S7C). Furthermore, PPN stimulation increased the number of foot slips (Figures 6E and 6F; Video S2), whereas the number of rearing events decreased (Figure S7D), suggesting disrupted sensorimotor integration. This effect likely contributed to the markedly reduced exploration of the grid area observed only in mice of the PPN group. The opposite effect in foot slips was observed during optogenetic inhibition of PPN glutamatergic neurons (i.e., decrease in foot slips), although similar to open-field locomotion data, the changes were not significant (Figure S6C). Stimulation of CnF neurons (n = 6 mice) resulted in mice jumping off the grid as a consequence of the robust motor activation, despite using lower frequencies

and lower laser power; therefore, these experiments were not quantified. Altogether, these results indicate that activation of CnF glutamatergic neurons produced motor responses with no voluntary control, i.e., regardless of the behavioral context, and the intensity of the response was only determined by the frequency of stimulation. However, activation of PPN glutamatergic neurons blocked distinct components of motor activity regardless of the frequency of stimulation, including locomotion and gait.

Differential modulation of muscle activity by PPN and CnF neurons

Classically, the function that defines the MLR is the modulation of locomotion. Despite both PPN and CnF providing excitatory innervation to motor structures in the lower brainstem, medulla, and spinal cord, the effect of activating each neuronal group separately revealed contrasting effects during motor behavior. To determine whether the seemingly opposing effects on locomotion reflect a competing process between PPN and CnF neurons or a cooperative mechanism to produce an integrated motor output, we measured the impact of each group of neurons on muscles involved in locomotion. VGLUT2-cre mice were unilaterally transduced with ChR2 in either the PPN (n = 4) or the CnF (n = 4; control wild type, n = 3) and were bilaterally implanted with bipolar electromyogram (EMG) electrodes in both the forelimb and the hindlimb biceps. Mice were recorded during spontaneous behavior in their home cage, and single blue light pulses (20 ms) were randomly delivered (Figure 7A). First, we measured the effect on the muscle tone and found that blue light stimulation equally induced an increase in the EMG signal in the PPN and CnF groups but followed different dynamics: CnF stimulation transiently increased the root-mean-square (RMS) signal, resulting in short muscular activation, whereas PPN stimulation produced a long-lasting contraction (response duration: PPN: 1,383.59 ± 59.50 ms; CNF: 384.91 ± 15.71 ms; Figures 7B and 7C). The analysis of the first 500 ms after the onset of the blue laser revealed that the magnitude of the responses between PPN and CnF groups is similar (percentage of change, 0–0.5 s; PPN: 193.988 ± 13.504, CnF: 213.378 ± 29.346, CTRL: −5.24 ± 4.21; one-way ANOVA: $F_{(2,214)} = 4.89$, $p = 0.0084$; post hoc Bonferroni: $P_{PPN\text{-}CTRL} = 0.017$, $P_{PPN\text{-}CNF} = 0.9$, $P_{CNF\text{-}CTRL} = 0.006$), but the difference becomes evident following this initial phase, denoting a long-lasting effect in the PPN group (percentage of change 0.5–2 s; PPN: 78.60% ± 10.06%, CnF: 15.72% ± 3.93%, CTRL: 6.66% ± 4.55%; one-way ANOVA, $F_{(2,214)} = 26.26$, $p = 0.00001$; post hoc Bonferroni: $P_{PPN\text{-}CTRL} = 0.0001$, $P_{PPN\text{-}CNF} = 0.0001$, $P_{CNF\text{-}CTRL} = 0.04$; Figures 7B and 7C). Furthermore, the response latency following PPN stimulation was significantly shorter than in the CnF group (PPN: 28 ± 4.78 ms, CNF: 79.45 ± 10.58 ms; two-tailed t test: $t_{(211)} = -3.58$, $p = 0.0004$; Figure 7D). These results suggest that PPN stimulation produces a robust and long-lasting effect on the muscle tone, contrasting with a short-lasting effect that follows the stimulation of the CnF.

We next evaluated the effect of the stimulation on the contralateral musculature. Stimulation of PPN neurons produced a marked increase in the amplitude of the ipsilateral biceps that was significantly larger than that of the contralateral biceps. In contrast, stimulation of CnF neurons produced similar increases in the EMG amplitude of the ipsilateral and contralateral biceps (Figures 7E and 7F; Figures S7E–S7G). Thus, although activation of PPN neurons produces a long-lasting increase in the amplitude of the ipsilateral EMG consistent with increased muscle resistance to passive movement, the bilateral nature of the short-lasting

muscle activation observed after unilateral CnF stimulation is consistent with the frequency-dependent bouts of locomotor activity. Further evidence was obtained following CnF low-frequency (0.1 Hz) or high-frequency (5 Hz) stimulation while mice were held in a tail-lifted position, revealing motor contractions that resemble context-independent involuntary locomotion (Video S3). In contrast, the lasting increase in muscle tone observed following PPN stimulation may act as a readiness signal that precedes locomotion, possibly associated with posture, suggesting that both MLR structures act in coordination to modulate the motor output. These results, together with the differences in connectivity and physiological properties, uncover fundamental differences in the modulation of muscle activity by MLR neurons and reveal their differential roles in motor behavior.

DISCUSSION

Neurons of the MLR have been classically identified as a critical node for the integration of behavioral signals originating in forebrain systems related to the modulation of motor output. The results presented in this study reveal several differences among MLR substructures in terms of their connectivity, physiological properties, and effects on motor behavior and muscle activity. In terms of connectivity, we show that PPN neurons have widespread projections to various motor regions, including the basal ganglia and spinal cord, whereas CnF neurons have a more restricted spread of efferents. In terms of physiological properties, we show that PPN neurons comprise a heterogeneous group displaying a range of adapting responses, whereas most CnF neurons are fast adapting. In terms of behavior, we show that stimulation of PPN neurons decreases overall motor activity, whereas CnF stimulation produces robust and highly reliable bouts of motor activity. Finally, stimulation of PPN neurons produces a prolonged increase in muscle tone, whereas stimulation of CnF neurons produces brief, bilateral motor contractions of the limbs. Thus, the distinct attributes observed among MLR structures reveal major differences in their composition and properties and shed light onto the fundamental mechanisms underlying their role in motor behavior.

Our data reveal that CnF glutamatergic neurons control a stereotypical motor response that scales its intensity with optogenetic frequency; from high-velocity locomotion to jumping, CnF stimulation causes rapid movement of the hindlegs independent of context. Subsequently, we observed that these motor effects can be explained by fast, monophasic, and bilateral muscle responses that mostly occurred within the 0.25 s immediately following optogenetic CnF stimulation, in contrast with PPN stimulation, which caused multiphasic EMG fluctuations above baseline for an average of 1.5 s, sometimes longer than 2 s. Along with the swift and consistent effect of CnF stimulation on muscle and motor responses, we found that most CnF neurons (85.7%) are fast adapting and strongly accommodating, suggesting that they are capable of generating phasic motor responses to the synaptic drive by upstream structures. Predominant inputs to the CnF are the superior colliculus, inferior colliculus, and periaqueductal gray area, providing a basis for the rapid transmission of sensory information in contexts that signal threat. Along these lines, the only regions that showed a higher density of synaptophysin-positive axons from the CnF than the PPN were the hypothalamus (notably, the preoptic nucleus) and the habenula, regions involved in homeostatic regulation (Augustine et al., 2018; Zhao et al., 2017) and the valuation of threat

(Amo et al., 2014; Hikosaka, 2010), respectively. Overall, our data support a developing theory that the CnF is involved in fast-escape behavior (Caggiano et al., 2018; Gatto and Goulding, 2018), and its activity is likely to be modulated by fast-incoming sensory information.

In contrast to the CnF, we show that PPN glutamatergic neurons display heterogeneous features as revealed by a wider input/output connectivity map, a range of spike adaptation profiles, and distinct effects on motor behavior. Whereas the CnF exhibited a more restricted output domain, synaptophysin-positive PPN axons were observed in the spinal cord, medulla, midbrain, cerebellum, thalamus, basal ganglia, and cortex (although there are early reports of a possible projection from the CnF to the spinal cord; (Castiglioi et al., 1978; Liang et al., 2011; Satoda et al., 2002). Notably, every brain region that provides input neurons projecting to the CnF also provides input to the PPN. Of the neurons we recorded in the PPN, 48.8% were fast-adapting neurons, 30.2% were non-adapting neurons, and 21% were slow-adapting neurons, suggesting a greater diversity of neuronal profiles than in the CnF. In terms of behavior, PPN stimulation causes stopping in the open field and on the treadmill, with no significant relationship to the 10- and 20-Hz stimulation frequencies used. These findings agree with prior studies that have shown decreased locomotion (Josset et al., 2018) or no increase in locomotion (Caggiano et al., 2018) due to PPN stimulation at these frequencies (but see Caggiano et al., 2018, for the effect at higher frequencies). Furthermore, we found that stopping behavior was not the only PPN-dependent phenomenon observed. For instance, on the elevated grid walk test, PPN stimulation led to not only decreased travel distance and more time in the center of the grid but also significantly more foot slips, which could be interpreted in the context of a loss of motor coordination (as seen in lesions to PPN cholinergic neurons; (Maclaren et al., 2014)) or reset of the motor action sequence (potentially through activation of striatal interneurons; Assous et al., 2019). Nevertheless, an alternative mechanistic interpretation based on the EMG data suggests that PPN neurons increase muscle tone in preparation for movement (i.e., posture) but lack the capability of triggering motor output by themselves. In agreement with Josset et al. (2018), our results show a bilateral effect on flexor muscles (biceps). In their study, the authors report that the effect of CnF stimulation is indicative of an acceleration of step cycles, whereas the effect of PPN stimulation is explained as an increase in the stance phase duration because of a phasic response in the flexor muscles, thus compatible with the prolonged increase in muscle tone reported here that would consequently disrupt the step cycle. Compared with CnF-derived muscle responses, PPN stimulation caused EMG activation events that were multiphasic and 6 to 8 times longer on average and produced increases from baseline that were 3 times larger. Although short-lived CnF muscle activation was tightly correlated with locomotion bouts, PPN muscle activation was not. Thus, the effect of PPN stimulation on the EMG revealed a prolonged increase in muscle tone in the absence of movement that is consistent with the muscle preparation that would be necessary to execute upstream-driven (e.g., basal ganglia) motor commands. Such interpretation is congruent with the activity of PPN glutamatergic neurons in arousal and behavioral activation (Petzold et al., 2015; Boucetta et al., 2014; Kroeger et al., 2017), suggesting that PPN neurons encode a readiness signal that enables motor responses. Altogether, our results uncover aspects of the heterogeneity observed in PPN glutamatergic neurons (Roš et al., 2010), which will hold important clues

to understanding their multifarious contributions to behavior and highlight the necessity of future studies to address this in detail. Together with two recent publications characterizing the MLR function (Caggiano et al., 2018; Josset et al., 2018), our results support the involvement of MLR neurons in distinct aspects of locomotion that rely on specific subsets of excitatory neurons with distinct connectivity patterns.

Growing evidence shows that the function of PPN neurons is closely linked to the basal ganglia. For example, PPN glutamatergic neurons are capable of reliably patterning dopamine release via synapses targeting the soma, proximal dendrites, and axon initial segment of SNc dopamine neurons (Galtieri et al., 2017). Furthermore, PPN glutamatergic neurons innervate striatal interneurons and produce feed-forward inhibition of striatal output (Assous et al., 2019). In addition to the SNc and the striatum, our data revealed synaptophysin-positive axons in the globus pallidus, entopeduncular nucleus, SNr, and VTA originating in the PPN. In comparison, the CnF only projects to the VTA, SNr, and globus pallidus. Altogether, basal ganglia structures receive a greater density of axons from the PPN than the CnF. The PPN also exclusively targets the CM-Pf thalamus, which exhibits strong control on the basal ganglia by gating inputs to the striatum before the selection of goal-directed actions (Minamimoto et al., 2009, 2014), signaling saliency (Matsumoto et al., 2001), and controlling the learning of new action-outcome contingencies (Bradfield et al., 2013) by affecting striatal microcircuitry via control of specific interneuron subpopulations (Bradfield et al., 2013; Assous et al., 2017). In terms of afferent connectivity, our data show that every node of the basal ganglia provides input to the MLR (predominantly to the PPN). In particular, neurons of the SNr, which constitute the main basal ganglia output in rodents, are among the primary structures providing input to the PPN, but not the CnF, as revealed by ourselves and others (Caggiano et al., 2018; Roseberry et al., 2016). Nevertheless, despite the close bidirectional connectivity and functional analogy between the PPN and the basal ganglia, our data reveal that the input/output connectivity map of PPN glutamatergic neurons is far more distributed and intricate than previously considered. This suggests that several other brain regions may converge on basal ganglia output-recipient PPN neurons, thus conferring them with the potential to weigh the distinct synaptic inputs and select an integrated behavioral output.

In the past decade, the PPN has emerged as a potential target for deep brain stimulation (DBS) with a mixture of results, thus rendering its use controversial (Albin et al., 2018). Our work suggests that the variability observed in the clinical setting may partly result from differences in electrode location and/or stimulation frequency and intensity. Although investigations of the two excitatory structures comprising the MLR provide insight toward a general model, the complexity of the MLR input/output map suggests a topography of domain-specific subnetworks that must be examined specifically to interpret the variability observed following PPN-DBS in clinical populations. The variety of observed motor effects due to MLR stimulation between our study and others (Caggiano et al., 2018; Roseberry et al., 2016) is likely a manifestation of different PPN subcircuits being recruited because of varying experimental manipulations (i.e., fiber optic location, extension of the ChR2 transduction area, and/or stimulation frequency and intensity). One possibility could be that the strong effects that the PPN has on dopamine release are only recruited under specific stimulation parameters and provide a basis for exploratory locomotion (e.g., Xiao et al.,

2016), whereas other PPN glutamatergic circuits modulate muscle tone. An alternative explanation is that over-recruitment of segregated PPN pathways by optogenetics results in stopping. Pathway-specific interventions controlled by stimulation site, frequency, or intensity could provide a new dimension by which to analyze the MLR as a versatile DBS target.

STAR⋆METHODS

RESOURCE AVAILABILITY

Lead contact—Further information and requests for resources and reagents should be directed to and will be fulfilled by the lead contact, Juan Mena-Segovia (juan.mena@rutgers.edu).

Materials availability—No unique reagents were generated in this study.

Data and code availability

- All data reported in this paper will be shared by the lead contact upon request.
- No original code was generated in this paper.
- Any additional information required to reanalyze the data reported in this paper is available from the Lead Contact upon request.

EXPERIMENTAL MODEL AND SUBJECT DETAILS

Heterozygous floxed tdTomato (B6;129S6-Gt(ROSA)26Sortm9(CAG-tdTomato)Hze/J; Jax number: 007905), VGLUT2-cre (Slc17a6tm2(cre)Lowl (also called VGLUT2-ires-Cre); Jax number: 028863), and wild-type (C57BL/6, Jax number: 000664) adult male and female mice (2–6 months old) were used for all experiments. All mice were housed on a normal 12:12h light:dark cycle (light on at 7:00) and had unrestricted access to food and water. All experiments were performed in accordance with the National Institutes of Health Guide to the Care and Use of Laboratory Animals, and the Hungarian and International EU Directive 2010/63/EU for all animal experiments. Approval was obtained from Rutgers University Institutional Animal Care and Use Committee (16054A1D0819) and the Committee of Animal Research of the University of Debrecen (5/2015/DEMAB).

METHOD DETAILS

Viral Injections/Surgery—All surgeries were performed under aseptic conditions. Body temperature was maintained at 37 ± 1°C using a heating pad. Mice were deeply anesthetized with isoflurane (1.5% to 4%, in O_2) and placed in a stereotaxic apparatus (David Kopf Instruments). Ophthalmic ointment was applied. Following skin incision, a small cranial hole was made above the targeted area. All measurements were made relative to bregma and dorsoventral coordinates were set from dura. Viral injections were performed using a 32-gauge syringe (Hamilton Syringes Neuros, #65458) at 5–7 nl/min rate using a microsyringe pump (micro4, WPI). For multiple injections, an additional syringe was used to avoid contamination, and syringes were thoroughly cleaned with ethanol and water between each experiment. After completion of the injections, 10 to 15 min were allowed before

slowly withdrawing the syringe. At the end of the surgeries, animals received injections of Buprenorphine (0.10mg/kg, sc) and Baytril (0.05mg/kg). Viruses used for all experiments were as follows: AAV2-DIO-EF1α-YFP (titer: 10^12; injection in PPN: 20nL; injection in CnF: 15nL, UNC Vector Core); AAV2-DIO-EF1α-YFP-2A-synaptophysin-mRuby (titer: 10^12; injection in PPN: 10nL; injection in CnF: 10nL, Stanford Vector Core); AAV5-DIO-TVA-mCherry (titer: 10^12; injection in PPN: 10nL, injection in CnF: 7.5nL, UNC Vector Core); AAV8-DIO-RG (titer: 10^12; injection in PPN: 10nL, injection in CnF: 7.5nL, UNC Vector Core); RvDG-YFP (titer: 10^8; injection in PPN: 200nL, injection in CnF: 200nL, Salk Institute), AAV2-Flex-EF1a-ChR2(H134R) (titer: 10^12; injection in PPN: 20nL, injection in CnF: 15nL UNC Vector Core). Injection were delivered in the following coordinates (in mm from Bregma): PPN: AP: −4.5, ML: ± 1.25, DV: 3.3; CnF: AP: −5.0, ML: ± 1.2, DV: 2.2.

Histology—After *in vivo* experimental procedures were completed, animals were deeply anesthetized with sodium pentobarbital (200 mg/kg) and transcardially perfused with 20ml of phosphate buffer solution (PBS 0.05M) followed by 20ml of paraformaldehyde (PFA 4%). The entire brain and the spinal cord were removed and post-fixed in PFA for 12h. Before slicing, the brain was embedded in a single block of Agar (in PBS, 2%) as well as 3–5mm sections of the spinal cord that were collected in anteroposterior order. Spinal cord and brain sections were sliced at 50μm following coronal or sagittal axes and collected in individual well-plates with 300μm spacing between sections. All immunohistochemistry solutions were prepared in a solution of PBS with 0.3% Triton (PBS-Triton). First, sections were blocked in PBS-Triton containing 10% normal donkey serum (NDS, Jackson Immunoresearch) for 1h at room temperature, following 3–5 washes with PBS, sections were transferred in a primary antibody solution containing PBS-Triton, 1% NDS and the corresponding primary antibody. The primary solution was left overnight at 4°C under constant gentle shaking. Sections were then washed 3–5 times with PBS before being transferred to the secondary antibody solution (PBS Triton, 1% NDS, and the corresponding secondary antibody) and kept under constant gentle shaking for 4–5h at room temperature. Sections were then washed 3–5 times in PBS before mounted on microscope slides using a mounting medium (Vectashield) and prepared for imaging. Primary antibodies were as follows: mCherry (used for mRuby, mCherry and TdTomato, made in mouse, monoclonal, ABCAM AB167477, dilution 1:1000), ChAT (choline acetyltransferase, made in goat, polyclonal, Merk Millipore, AB144P, dilution 1:500), GFP (to enhance eYFP detection, made in rabbit, polyclonal already conjugated-488, Thermofisher, A21311, dilution 1:1000) and Fluorogold (made in rabbit, polyclonal, Merck Millipore, AB153-I, dilution 1:1000). Secondary antibodies were as follows: anti-Goat CY3 (raised in donkey, Jackson Immuno-research 705–165-147, dilution 1:1000), anti-Goat CY5 (raised in donkey, Jackson Immuno-research 705–175-147, dilution 1:1000), anti-mouse CY3 (raised in donkey, Jackson Immuno-research 715–165-150, dilution 1:1000), anti-rabbit 488 (raised in donkey, Jackson Immuno-research 711–545-152, dilution 1:1000) and anti-rabbit AMCA (raised in donkey, Jackson Immunoresearch 711–155-152, dilution 1:1000).

Imaging—Fluorescent images were captured using a confocal laser microscope (Olympus FV2000) with the FluoView software (Olympus), under a dry 10X/0.40 NA objective,

20X/0.40NA objective or an oil-immersion 63X/1.40NA objective. All sections were first acquired at high resolution (10X, 1024 * 1024 pixels) using mosaic reconstruction to determine the virus diffusion, the viral injection site and the placement of the optic fiber. For cell counting, sections were scanned at 20X using medium resolution (1048 * 720). For projections and synapses counting, sections were acquired at high resolution (20X, 2048 *2048 pixels), with a 1μm-optical section z stack across 40μm (top and bottom 5μm of the section were discarded). Single images of axonal projections or synaptic contacts were acquired at high magnification (63X), high-resolution (2048*2048 pixels), with 4-time deconvolution and a 1μm-optical section z stack across 40μm. All pictures were saved as images and metadata in order to correct the mosaic alignment using Photoshop (version 5, Adobe). All fluorescent images were transferred to Fiji software, were color-converted based on the secondary antibody and the filter used (AMCA: 400 – 450 nm, Alexa488: 500–550 nm, CY3: 590–620 and CY5: 650–700), signal-adjusted, and merged using in-built tools.

Cell counting—Each brain and spinal cord section scanned were converted into bitmap images, duplicated and overlapped with the outline of the (Franklin and Paxinos, 2019), mouse brain Atlas (7th edition). Images were then transferred to Fiji, and in-built counting tools were used. The number of cell markers per nucleus (as defined by the Atlas) was then transferred to an Excel spreadsheet. The counted cells of each identified brain structure that were represented in separate sections were put together for the final analysis and normalized to the total number of neurons counted in all brain sections collected for each animal. For RvdG experiments, the YFP-positive neurons located in the site of injection (PPN/CnF) were not quantified for the whole brain mapping. For the spinal cord, a random number of spinal cord sections that were representative of all segments (40–80 sections per mice) were processed and counted. Based on the average number of inputs neurons per section found, we extrapolated the putative number of inputs in the entire spinal cord using an average length of 3.2cm. Normalized data and raw data were tested for normality and compared using a Wilcoxon rank-sum test (non-parametric). The threshold to significance was determined at $p < 0.05$. All data were shown as mean ± SEM.

Synapse density estimation—Brain sections were prepared as above. For each brain section, the signals of both fluorescent proteins (YFP and mRuby) were normalized to the overall signal in the entire section (background) and to the signal outside the section (periphery). This approach allowed us to normalize the fluorescent signal to the overall background. Next, we outlined each brain structure using in-built tools (see below), and the number of pixels above threshold, the surface area, and the average gray value within the drawing area were obtained to define the density of the synapses using the formula: *(average gray value – background gray value)/surface area.*

The area that was considered as an artifact due to dust or air-bubbles generated during immunohistochemistry or slice mounting was manually discarded using a similar approach. For each brain structure, the border was defined using the contour function of imageJ and the surface was extracted for each structure on each section. Next, the scans of the mRuby and the YFP signals were apposed, and the number of overlapping pixels were considered as synapses labeled by the viral injections (yellow pixels were converted into gray scale).

This allowed us to remove YFP-only signal that was considered as fibers en-passage and mRuby-only signal that was considered as artifacts. For each structure, the number of pixels and the surface area were then converted into pixel density. For each mouse, 1 slice every 300μm was analyzed to provide an optimal coverage of the entire brain. Because the same structure can be present on several slices, pixel densities were averaged for each structure in the same mouse before comparing them between mice.

Normalized data and raw data were tested for normality and compared using a Wilcoxon rank-sum test (non-parametric). The threshold for significance was defined at $p < 0.05$. All data were shown as mean ± SEM.

***Ex vivo* Electrophysiology—**9–16 days old animals expressing tdTomato fluorescent protein in a VGLUT2-dependent way (n = 25) were used for the slice electrophysiology experiments. Coronal midbrain slices (with 200 μm thickness) were prepared in low Na^+ aCSF (cca. 0 to −2°C) with a Microm HM 650V vibratome (Microm International GmbH, Walldorf, Germany). The slices were incubated in normal aCSF for 1 hour on 37°C prior to starting the experiment. The resistance of the patch pipettes was 5–7 MΩ, and the composition of the internal solution was the following (in mM): K-gluconate, 120; NaCl, 5; 4-(2-hydroxyethyl)-1- piperazineethanesulfonic acid (HEPES), 10; Na2- phosphocreatinine, 10; EGTA, 2; CaCl2, 0.1; Mg-ATP, 5; Na3-GTP, 0.3; biocytin, 8; pH 7.3. Whole-cell patch-clamp experiments were conducted at room temperature with an Axopatch 200A amplifier (Molecular Devices, Union City, CA, USA). Clampex 10.0 software (Molecular Devices, Union City, CA, USA) was used for data acquisition, while data analysis was performed by Clampfit 10.0 (Molecular Devices) software. Only stable recordings with minimal leak currents were considered, and only recordings with series resistance below 30 MΩ, with less than10% change, were included. Both voltage- and current clamp configurations were employed. Protocols and recorded parameters are represented in Table S1. In certain experiments, 1 μM tetrodotoxin (TTX; Alomone Laboratories, Jerusalem, Israel) was administered in the bath to eliminate action potential generation in the preparation. Visualization of the genetically encoded fluorescent marker (tdTomato) was achieved by using a fluorescent imaging system (Till Photonics GmbH, Gräfeling, Germany) containing a xenon bulb-based Polychrome V light source, a CCD camera (SensiCam, PCO AG, Kelheim, Germany), an imaging control unit (ICU), and the Till Vision software (version 4.0.1.3).

Morphological analysis of the recorded neurons: Patched neurons were labeled with biocytin and samples were fixed (4% paraformaldehyde in 0.1 M phosphate buffer; pH 7.4; 4°C) for morphological identification of the neurons. Tris-buffered saline (in mM, Tris base, 8; Trisma HCl, 42; NaCl, 150; pH 7.4) supplemented with 0.1% Triton X-100 and 10% bovine serum (60 min) was used for permeabilization. Incubation was performed in phosphate buffer containing streptavidin-conjugated Alexa488 (1:300; Molecular Probes Inc., Eugene, OR, USA) for 90 min. The cells were visualized using a Zeiss LSM 510 confocal microscope (Carl Zeiss AG). The reconstruction of neurons was performed by NeuroLucida software (MBF Bioscience, Williston, VT, USA).

Behavioral assays

Laser stimulation: A blue laser (473nm, OEM Laser system) was used to excite ChR2, and a yellow laser (589nm, OEM Laser system) was used to excite NpHR3.0. Stimulation parameters varied. Several stimulation frequencies were used (1Hz-20z) and controlled by a low-noise shutter (SH1, Thorlabs) plugged to the control cube (KSC101, Thorlabs) which in turn was triggered by TTL signals delivered by the Anymaze interface. The laser output was set to be 2–3 mW at the end of the patchcord. For all ChR2 stimulations, the laser parameters were as follows: Laser ON (pulses of 20ms at various frequency for 1 s) and Laser OFF (inter-stimulation interval of 9 s). For NpHR3.0 stimulation, laser delivery was continuous one min.

Small Open field: Following implantation of the optic fiber, animals were allowed to recover for 5 to 7 days. Animals were then habituated for 5 minutes to the open field before testing. The custom-made open field was developed as following: a dark cube of 40 × 40 × 40 cm with the floor covered with a non-reflective white surface to allow better contrast between the background and the mouse, 4 white lamps were positioned on the top of the cage to allow optimal illumination. Animals were tested for 30 minutes, with optogenetic stimulation 1 s ON/9 s OFF (20ms pulses, < 3mW laser power) using stimulation frequencies of 1, 10 or 20Hz. The animal movements were recorded using a high-speed/high-resolution camera (120fps) RunCam2 and the software Anymaze (Stoelting). The software was tracking the gravity center (body) of the animal, the head and the tail position. The time in the center (15cm circle located in the center of the field) or periphery was defined based on the position of the animal body. The software recorded the animals' speed, distance traveled, time in center and time in the periphery in 5 ms bins. While online analyses of the above-mentioned parameters were based on 30 recorded frames per second, offline analyses used 120 frames per second. On-and offline analyses were compared and sequences differing in more than 5% were discarded. Stimulation delivery was controlled using the software interface Ami1.

Large open field: The above experiment was repeated in a larger open field, which consisted of a dark cube of 80 × 80 × 80 cm with the same features as the one described above. A small slope was built at the base of each wall to avoid animals making contact with the walls. Animals were tested for 60 minutes, optogenetic stimulations were delivered for 1 minute (repeated loops of 1 s ON/9 s OFF on) and were spaced by 1 minute with no stimulation. Stimulation protocol was as follow: 20ms pulses, < 3mW laser power and the frequency was increased from 0.1 to 30 Hz (0.1, 0.5, 1, 2.5, 5, 7.5, 10, 12.5, 15, 17.5, 20, 22.5, 25, 27.5, 30). Animals movement were recorded and analyzed as above.

Treadmill: The treadmill apparatus consists of a custom-made belt of 10cm by 30cm that is operated at constant speed. The animals' position, the center of the body, head, and tail were monitored using the Anymaze software via a high-speed camera (RunCam2) camera placed above the treadmill. Further, the behavior was also monitored using a camera located on the side of the treadmill. Animals were tested for 15 minutes while receiving optogenetic stimulation (1 s ON/9 s OFF, 20ms pulses, < 3mW, 10Hz). 2 days before testing, animals were habituated to the still treadmill for 10 minutes. One day before testing, the habituation

occurred on the moving treadmill. On the day of testing, animals were connected to the laser and placed on the treadmill with the speed set at 3 m per minute. Animals were tracked and analyzed to determine distance traveled, average speed and position of the head-body and tail-body axes. Stimulation delivery was controlled using the software interface Ami1.

Elevated grid: The elevated grid apparatus consists of a custom made 20 × 40 cm grid (1.5 × 1.5 cm grid space), elevated off the floor and illuminated from the bottom. The animals' behavior was monitored by two high speed-cameras located on the side (for rearing and foot slips) and on the bottom (for the animal position). Animals were not exposed to the apparatus before testing to avoid any habituation, but all animals were handled for several days before testing. On the day of the testing, animals were connected to the laser, placed in the middle of the grid and their behavior was monitored for 20min using Anymaze software while receiving optogenetic stimulation for 1 s every 9 s (20ms pulses, < 3mW, 10Hz). Animals were tracked and analyzed to determine distance traveled, average speed and position of the head-body and tail-body axes. Stimulation delivery was controlled using the software interface Ami1.

Control animals: For each experiment, control animals consisted of WT animals receiving the same manipulations and undergoing the same procedures as the experimental groups. Control animals were excluded if the injection was "out-of-target" or the implantation was not correctly positioned.

High-resolution analyses: The cartesian coordinates of each acquired frame (120 fps) were converted offline into interframe distance traveled. The peristimulation distance traveled was defined as the "stimulation locked distance traveled" using z-score transformation normalized into the 5 s baseline prior to each stimulation. Due to camera fps variability, the cartesian coordinates were used at 5ms intervals by extrapolating the interframe position.

Data analyses: All experiments were randomly organized, and data of each animal were analyzed similarly. To prevent data loss during animal tracking, the data from online and offline were compared, and the portion of data was removed if we found any differences in the recording. Following comparison of the online/offline tracking, data were expressed as the following parameters: overall distance traveled, average speed during the entire session, number of ipsilateral or contralateral rotations, and distance traveled 5 s before and after each stimulation (with 5ms bin size). High-resolution data were converted to z-score of the distance traveled compared to the baseline (−5 to 0 s before stimulation). All data were compared between groups using one-way ANOVA or by comparing the frequency of stimulation and groups using multivariate ANOVA. A significant ANOVA effect was compared using Bonferroni post hoc analysis.

Electromyogram recordings—During a surgical procedure as described above, an incision was made at the neck, forelimbs and hindlimbs of the animals and muscles were exposed. EMG bipolar electrodes were implanted in the biceps brachia and biceps femoris of the ipsilateral and contralateral limbs and the connector was affixed on the skull of the animals. In addition, an optic fiber (flat-cut, 200μm, 0.50NA) was implanted above the PPN or CnF (300μm above the injection site) following viral injections and maintained

in position using anchor screws. EMG signals were converted into RMS signal and each trial was analyzed individually. All animals received same number of stimulation to avoid overrepresentation.

Histological verification—Following staining of sections located in the vicinity of the injection sites for GFP and ChAT, high-resolution images were acquired and processed using Fiji. All ChAT-positive neurons located at the border of the PPN were labeled using in-built tools, then all YFP-positive cell bodies were labeled and their location recorded. The number of YFP-positive neurons located further than 100μm from the closest ChAT-positive neurons (for PPN and the ventral border of the CnF), or within the colliculus (for the dorsal border of the CnF) was calculated as a percentage of the total number of neurons within the injection site. If more than 5% of YFP-positive neurons were located further than 100μm (for PPN) or closest to 100μm or inside the colliculus (for CnF) the animal was excluded from further analyses.

QUANTIFICATION AND STATISTICAL ANALYSIS

Anatomical, *in vitro* and *in vivo* data (including behavioral data) are represented as mean ± SEM. No power analyses were conducted prior to the experiments and group sizes were determined following comparable previously published experiments. Anatomical data was compared using the Wilcoxon rank-sum test following prior determination of the violation of the assumption of normality of the data. *In vitro* data was analyzed using Student's t test, one-way ANOVA or mixed ANOVA. One-way ANOVAs and MANOVAs were conducted for *in vivo* and behavioral experiments. All ANOVAs were followed by Bonferroni corrected post hoc tests. Level of significance was set at $p < 0.05$. P values and sample sizes can be found in the Results section and the figure legends.

Supplementary Material

Refer to Web version on PubMed Central for supplementary material.

ACKNOWLEDGMENTS

This research was supported by NIH grant NS100824 (to J.M.-S.), NJ-DOH grant CSCR20IRG008 (to J.M.-S.), a NARSAD Young Investigator Award (to J.M.-S.), the Hungarian National Brain Research Program (to B.P.), the OTKA Bridging Fund of the University of Debrecen (to B.P.), and Rutgers University. The authors are grateful to Dr. Péter Szücs (Department of Anatomy, Histology and Embryology, Medical Faculty, University of Debrecen) for providing access and for his help in Neurolucida reconstructions and Prof. Miklós Antal (Department of Anatomy, Histology and Embryology, Medical Faculty, University of Debrecen) for providing VGLUT2-cre mice for breeding. The authors also thank Dr. Nadine Gut for comments on this manuscript.

REFERENCES

Albin RL, Surmeier DJ, Tubert C, Sarter M, Mὺller MLTM, Bohnen NI, and Dauer WT (2018). Targeting the pedunculopontine nucleus in Parkinson's disease: Time to go back to the drawing board. Mov Disord. 33, 1871–1875. 10.1002/mds.27540. [PubMed: 30398673]

Amo R, Fredes F, Kinoshita M, Aoki R, Aizawa H, Agetsuma M, Aoki T, Shiraki T, Kakinuma H, Matsuda M, et al. (2014). The habenulo-raphe serotonergic circuit encodes an aversive expectation value essential for adaptive active avoidance of danger. Neuron 84, 1034–1048. 10.1016/j.neuron.2014.10.035. [PubMed: 25467985]

Assous M, Kaminer J, Shah F, Garg A, Koós T, and Tepper JM (2017). Differential processing of thalamic information via distinct striatal interneuron circuits. Nat. Commun. 8, 15860. 10.1038/ncomms15860. [PubMed: 28604688]

Assous M, Dautan D, Tepper JM, and Mena-Segovia J (2019). Pedunculopontine Glutamatergic Neurons Provide a Novel Source of Feedforward Inhibition in the Striatum by Selectively Targeting Interneurons. J. Neurosci. 39, 4727–4737. 10.1523/JNEUROSCI.2913-18.2019. [PubMed: 30952811]

Augustine V, Gokce SK, Lee S, Wang B, Davidson TJ, Reimann F, Gribble F, Deisseroth K, Lois C, and Oka Y (2018). Hierarchical neural architecture underlying thirst regulation. Nature 555, 204–209. 10.1038/nature25488. [PubMed: 29489747]

Bajic D, and Proudfit HK (2013). Projections from the rat cuneiform nucleus to the A7, A6 (locus coeruleus), and A5 pontine noradrenergic cell groups. J. Chem. Neuroanat. 50–51, 11–20. 10.1016/j.jchemneu.2013.03.001.

Bordas C, Kovacs A, and Pal B (2015). The M-current contributes to high threshold membrane potential oscillations in a cell type-specific way in the pedunculopontine nucleus of mice. Front Cell Neurosci. 9, 121. 10.3389/fncel.2015.00121. [PubMed: 25904846]

Boucetta S, Cissé Y, Mainville L, Morales M, and Jones BE (2014). Discharge profiles across the sleep-waking cycle of identified cholinergic, GABAergic, and glutamatergic neurons in the pontomesencephalic tegmentum of the rat. J. Neurosci. 34, 4708–4727. 10.1523/JNEUROSCI.2617-13.2014. [PubMed: 24672016]

Bradfield LA, Bertran-Gonzalez J, Chieng B, and Balleine BW (2013). The thalamostriatal pathway and cholinergic control of goal-directed action: interlacing new with existing learning in the striatum. Neuron 79, 153–166. 10.1016/j.neuron.2013.04.039. [PubMed: 23770257]

Caggiano V, Leiras R, Goñi-Erro H, Masini D, Bellardita C, Bouvier J, Caldeira V, Fisone G, and Kiehn O (2018). Midbrain circuits that set locomotor speed and gait selection. Nature 553, 455–460. 10.1038/nature25448. [PubMed: 29342142]

Capelli P, Pivetta C, Soledad Esposito M, and Arber S (2017). Locomotor speed control circuits in the caudal brainstem. Nature 551, 373–377. 10.1038/nature24064. [PubMed: 29059682]

Castiglioi AJ, Gallaway MC, and Coulter JD (1978). Spinal projections from the midbrain in monkey. J Comp Neurol. 178, 329–345. 10.1002/cne.901780208. [PubMed: 415074]

Chao OY, Pum ME, Li J-S, and Huston JP (2012). The grid-walking test: Assessment of sensorimotor deficits after moderate or severe dopamine depletion by 6-hydroxydopamine lesions in the dorsal striatum and medial forebrain bundle. Neuroscience 202, 318–325. 10.1016/j.neuroscience.2011.11.016. [PubMed: 22142899]

Dautan D, Huerta-Ocampo I, Witten IB, Deisseroth K, Bolam JP, Gerdjikov T, and Mena-Segovia J (2014). A major external source of cholinergic innervation of the striatum and nucleus accumbens originates in the brainstem. J. Neurosci. 34, 4509–4518. 10.1523/JNEUROSCI.5071-13.2014. [PubMed: 24671996]

Dautan D, Souza AS, Huerta-Ocampo I, Valencia M, Assous M, Witten IB, Deisseroth K, Tepper JM, Bolam JP, Gerdjikov TV, and Mena-Segovia J (2016a). Segregated cholinergic transmission modulates dopamine neurons integrated in distinct functional circuits. Nat. Neurosci. 19, 1025–1033. 10.1038/nn.4335. [PubMed: 27348215]

Dautan D, Hacioğlu Bay H, Bolam JP, Gerdjikov TV, and Mena-Segovia J (2016b). Extrinsic Sources of Cholinergic Innervation of the Striatal Complex: A Whole-Brain Mapping Analysis. Front. Neuroanat. 10, 1. https://www.ncbi.nlm.nih.gov/pubmed/26834571. [PubMed: 26834571]

Franklin KBJ, and Paxinos G (2019). The mouse brain in stereotaxic coordinates, 5th edition (Academic Press).

Futami T, Takakusaki K, and Kitai ST (1995). Glutamatergic and cholinergic inputs from the pedunculopontine tegmental nucleus to dopamine neurons in the substantia nigra pars compacta. Neurosci. Res. 21, 331–342. 10.1016/0168-0102(94)00869-H. [PubMed: 7777224]

Galtieri DJ, Estep CM, Wokosin DL, Traynelis S, and Surmeier DJ (2017). Pedunculopontine glutamatergic neurons control spike patterning in substantia nigra dopaminergic neurons. Elife 6, e30352. 10.7554/eLife.30352. [PubMed: 28980939]

Garcia-Rill E, Skinner RD, and Fitzgerald JA (1983). Activity in the mesencephalic locomotor region during locomotion. Exp. Neurol. 82, 609–622. 10.1016/0014-4886(83)90084-5. [PubMed: 6653713]

Garcia-Rill E, Houser CR, Skinner RD, Smith W, and Woodward DJ (1987). Locomotion-inducing sites in the vicinity of the pedunculopontine nucleus. Brain Res. Bull. 18, 731–738. 10.1016/0361-9230(87)90208-5. [PubMed: 3304544]

Gatto G, and Goulding M (2018). Locomotion Control: Brainstem Circuits Satisfy the Need for Speed. Curr. Biol. 28, R256–R259. 10.1016/j.cub.2018.01.068. [PubMed: 29558639]

Geisler S, and Zahm DS (2005). Afferents of the ventral tegmental area in the rat-anatomical substratum for integrative functions. J. Comp. Neurol. 490, 270–294. 10.1002/cne.20668. [PubMed: 16082674]

Goetz L, Bhattacharjee M, Ferraye MU, Fraix V, Maineri C, Nosko D, Fenoy AJ, Piallat B, Torres N, Krainik A, et al. (2019). Deep Brain Stimulation of the Pedunculopontine Nucleus Area in Parkinson Disease: MRI-Based Anatomoclinical Correlations and Optimal Target. Neurosurgery 84, 506–518. 10.1093/neuros/nyy151. [PubMed: 29846707]

Hepp DH, Ruiter AM, Galis Y, Voorn P, Rozemuller AJM, Berendse HW, Foncke EMJ, and van de Berg WDJ (2013). Pedunculopontine cholinergic cell loss in hallucinating Parkinson disease patients but not in dementia with Lewy bodies patients. J. Neuropathol. Exp. Neurol. 72, 1162–1170. 10.1097/NEN.0000000000000014. [PubMed: 24226265]

Hikosaka O (2010). The habenula: From stress evasion to value-based decision-making. Nat Rev Neurosci. 11, 503–513. 10.1038/nrn2866. [PubMed: 20559337]

Hirsch EC, Graybiel AM, Duyckaerts C, and Javoy-Agid F (1987). Neuronal loss in the pedunculopontine tegmental nucleus in Parkinson disease and in progressive supranuclear palsy. Proc. Natl. Acad. Sci. USA 84, 5976–5980. 10.1073/pnas.84.16.5976. [PubMed: 3475716]

Huerta-Ocampo I, Hacioglu-Bay H, Dautan D, and Mena-Segovia J (2020). Distribution of midbrain cholinergic axons in the thalamus. eNeuro 7, ENEURO.0454–19.2019. https://doi.org/ENEURO.0454-19.2019.

Jellinger K (1988). The pedunculopontine nucleus in Parkinson's disease, progressive supranuclear palsy and Alzheimer's disease. J. Neurol. Neurosurg. Psychiatry 51, 540–543. 10.1136/jnnp.51.4.540. [PubMed: 3379428]

Jenkinson N, Nandi D, Miall RC, Stein JF, and Aziz TZ (2004). Pedunculopontine nucleus stimulation improves akinesia in a Parkinsonian monkey. Neuroreport 15, 2621–2624. 10.1097/00001756-200412030-00012. [PubMed: 15570164]

Josset N, Roussel M, Lemieux M, Lafrance-Zoubga D, Rastqar A, and Bretzner F (2018). Distinct Contributions of Mesencephalic Locomotor Region Nuclei to Locomotor Control in the Freely Behaving Mouse. Curr. Biol. 28, 884–901.e3. 10.1016/j.cub.2018.02.007. [PubMed: 29526593]

Kang Y, and Kitai ST (1990). Electrophysiological properties of pedunculopontine neurons and their postsynaptic responses following stimulation of substantia nigra reticulata. Brain Res 535, 79–95. 10.1016/0006-8993(90)91826-3. [PubMed: 2292031]

Kim LH, Sharma S, Sharples SA, Mayr KA, Kwok CHT, and Whelan PJ (2017). Integration of Descending Command Systems for the Generation of Context-Specific Locomotor Behaviors. Front. Neurosci. 11, 581. 10.3389/fnins.2017.00581. [PubMed: 29093660]

Korte SM, Jaarsma D, Luiten PGM, and Bohus B (1992). Mesencephalic cuneiform nucleus and its ascending and descending projections serve stress-related cardiovascular responses in the rat. J. Auton. Nerv. Syst. 41, 157–176. 10.1016/0165-1838(92)90137-6. [PubMed: 1491112]

Kroeger D, Ferrari LL, Petit G, Mahoney CE, Fuller PM, Arrigoni E, and Scammell TE (2017). Cholinergic, Glutamatergic, and GABAergic Neurons of the Pedunculopontine Tegmental Nucleus Have Distinct Effects on Sleep/Wake Behavior in Mice. J. Neurosci. 37, 1352–1366. 10.1523/JNEUROSCI.1405-16.2016. [PubMed: 28039375]

Lau B, Welter ML, Belaid H, Fernandez Vidal S, Bardinet E, Grabli D, and Karachi C (2015). The integrative role of the pedunculopontine nucleus in human gait. Brain 138, 1284–1296. 10.1093/brain/awv047. [PubMed: 25765327]

Lavoie B, and Parent A (1994). Pedunculopontine nucleus in the squirrel monkey: cholinergic and glutamatergic projections to the substantia nigra. J. Comp. Neurol. 344, 232–241. 10.1002/cne.903440205. [PubMed: 7915727]

Lee AM, Hoy JL, Bonci A, Wilbrecht L, Stryker MP, and Niell CM (2014). Identification of a brainstem circuit regulating visual cortical state in parallel with locomotion. Neuron 83, 455–466. 10.1016/j.neuron.2014.06.031. [PubMed: 25033185]

Leonard CS, and Llinás R (1994). Serotonergic and cholinergic inhibition of mesopontine cholinergic neurons controlling rem sleep: An in vitro electrophysiological study. Neuroscience 59, 309–330. 10.1016/0306-4522(94)90599-1. [PubMed: 8008195]

Liang H, Paxinos G, and Watson C (2011). Projections from the brain to the spinal cord in the mouse. Brain Struct Funct 215, 159–186. 10.1007/s00429-010-0281-x. [PubMed: 20936329]

Maclaren DAA, Santini JA, Russell AL, Markovic T, and Clark SD (2014). Deficits in motor performance after pedunculopontine lesions in rats - impairment depends on demands of task. Eur J Neurosci. 40, 3224–3236. 10.1111/ejn.12666. [PubMed: 24995993]

Manaye KF, Zweig R, Wu D, Hersh LB, De Lacalle S, Saper CB, and German DC (1999). Quantification of cholinergic and select non-cholinergic mesopontine neuronal populations in the human brain. Neuroscience 89, 759–770. 10.1016/S0306-4522(98)00380-7. [PubMed: 10199611]

Martinez-Gonzalez C, Wang HL, Micklem BR, Bolam JP, and Mena-Segovia J (2012). Subpopulations of cholinergic, GABAergic and glutamatergic neurons in the pedunculopontine nucleus contain calcium-binding proteins and are heterogeneously distributed. Eur. J. Neurosci. 35, 723–734. 10.1111/j.1460-9568.2012.08002.x. [PubMed: 22356461]

Matsumoto N, Minamimoto T, Graybiel AM, and Kimura M (2001). Neurons in the thalamic CM-Pf complex supply striatal neurons with information about behaviorally significant sensory events. J Neurophysiol 85, 960–976. 10.1152/jn.2001.85.2.960. [PubMed: 11160526]

Mena-Segovia J, and Bolam JP (2017). Rethinking the Pedunculopontine Nucleus: From Cellular Organization to Function. Neuron 94, 7–18. 10.1016/j.neuron.2017.02.027. [PubMed: 28384477]

Minamimoto T, Hori Y, and Kimura M (2009). Roles of the thalamic CM-PF complex-Basal ganglia circuit in externally driven rebias of action. Brain Res Bull. 78, 75–79. 10.1016/j.brainresbull.2008.08.013. [PubMed: 18793702]

Minamimoto T, Hori Y, Yamanaka K, and Kimura M (2014). Neural signal for counteracting pre-action bias in the centromedian thalamic nucleus. Front Syst Neurosci. 8, 3. 10.3389/fnsys.2014.00003. [PubMed: 24478641]

Mitchell IJ, Clarke CE, Boyce S, Robertson RG, Peggs D, Sambrook MA, and Crossman AR (1989). Neural mechanisms underlying parkinsonian symptoms based upon regional uptake of 2-deoxyglucose in monkeys exposed to 1-methyl-4-phenyl-1,2,3,6-tetrahydropyridine. Neuroscience 32, 213–226. 10.1016/0306-4522(89)90120-6. [PubMed: 2586750]

Mori S, Shik ML, and Yagodnitsyn AS (1977). Role of pontine tegmentum for locomotor control in mesencephalic cat. J. Neurophysiol. 40, 284–295. 10.1152/jn.1977.40.2.284. [PubMed: 845624]

Nandi D, Aziz TZ, Giladi N, Winter J, and Stein JF (2002). Reversal of akinesia in experimental parkinsonism by GABA antagonist microinjections in the pedunculopontine nucleus. Brain 125, 2418–2430. 10.1093/brain/awf259. [PubMed: 12390969]

Nieuwenhuys R, and Puelles L (2016). Towards a New Neuromorphology (Springer International).

Nigro MJ, Mateos-Aparicio P, and Storm JF (2014). Expression and functional roles of Kv7/KCNQ/M-channels in rat medial entorhinal cortex layer II stellate cells. J. Neurosci. 34, 6807–6812. 10.1523/JNEURO-SCI.4153-13.2014. [PubMed: 24828634]

Pahapill PA, and Lozano AM (2000). The pedunculopontine nucleus and Parkinson's disease. Brain 123, 1767–1783. 10.1093/brain/123.9.1767. [PubMed: 10960043]

Perera T, Tan JL, Cole MH, Yohanandan SAC, Silberstein P, Cook R, Peppard R, Aziz T, Coyne T, Brown P, et al. (2018). Balance control systems in Parkinson's disease and the impact of pedunculopontine area stimulation. Brain 141, 3009–3022. 10.1093/brain/awy216. [PubMed: 30165427]

Petzold A, Valencia M, Pál B, and Mena-Segovia J (2015). Decoding brain state transitions in the pedunculopontine nucleus: cooperative phasic and tonic mechanisms. Front. Neural Circuits 9, 68. 10.3389/fncir.2015.00068. [PubMed: 26582977]

Puelles L (2019). Survey of Midbrain, Diencephalon, and Hypothalamus Neuroanatomic Terms Whose Prosomeric Definition Conflicts With Columnar Tradition. Front. Neuroanat. 13, 20. 10.3389/fnana.2019.00020. [PubMed: 30873012]

Roš H, Magill PJ, Moss J, Bolam JP, and Mena-Segovia J (2010). Distinct types of non-cholinergic pedunculopontine neurons are differentially modulated during global brain states. Neuroscience 170, 78–91. 10.1016/j.neuroscience.2010.06.068. [PubMed: 20603194]

Roseberry TK, Lee AM, Lalive AL, Wilbrecht L, Bonci A, and Kreitzer AC (2016). Cell-Type-Specific Control of Brainstem Locomotor Circuits by Basal Ganglia. Cell 164, 526–537. 10.1016/j.cell.2015.12.037. [PubMed: 26824660]

Satoda T, Matsumoto H, Zhou L, Rose PK, and Richmond FJR (2002). Mesencephalic projections to the first cervical segment in the cat. Exp Brain Res 144, 397–413. 10.1007/s00221-002-1047-3. [PubMed: 12021821]

Sherman D, Fuller PM, Marcus J, Yu J, Zhang P, Chamberlin NL, Saper CB, and Lu J (2015). Anatomical Location of the Mesencephalic Locomotor Region and Its Possible Role in Locomotion, Posture, Cataplexy, and Parkinsonism. Front. Neurol. 6, 140. 10.3389/fneur.2015.00140. [PubMed: 26157418]

Shik ML, Severin FV, and Orlovskiĭ GN (1966). [Control of walking and running by means of electric stimulation of the midbrain]. Biofizika 11, 659–666. [PubMed: 6000625]

Takakusaki K, Shiroyama T, and Kitai ST (1997). Two types of cholinergic neurons in the rat tegmental pedunculopontine nucleus: Electrophysiological and morphological characterization. Neuroscience 79, 1089–1109. 10.1016/s0306-4522(97)00019-5. [PubMed: 9219969]

Wang HL, and Morales M (2009). Pedunculopontine and laterodorsal tegmental nuclei contain distinct populations of cholinergic, glutamatergic and GABAergic neurons in the rat. Eur. J. Neurosci. 29, 340–358. 10.1111/j.1460-9568.2008.06576.x. [PubMed: 19200238]

Zweig RM, Whitehouse PJ, Casanova MF, Walker LC, Jankel WR, and Price DL (1987). Loss of pedunculopontine neurons in progressive supranuclear palsy. Ann. Neurol. 22, 18–25. 10.1002/ana.410220107. [PubMed: 3631916]

Xiao C, Cho JR, Zhou C, Treweek JB, Chan K, McKinney SL, Yang B, and Gradinaru V (2016). Cholinergic Mesopontine Signals Govern Locomotion and Reward through Dissociable Midbrain Pathways. Neuron 90, 333–347. 10.1016/j.neuron.2016.03.028. [PubMed: 27100197]

Zhao Z-D, Yang WZ, Gao C, Fu X, Zhang W, Zhou Q, Chen W, Ni X, Lin J-K, Yang J, et al. (2017). A hypothalamic circuit that controls body temperature. Proc Natl Acad Sci U S A 114, 2042–2047. 10.1073/pnas.1616255114. [PubMed: 28053227]

Zweig RM, Jankel WR, Hedreen JC, Mayeux R, and Price DL (1989). The pedunculopontine nucleus in Parkinson's disease. Ann. Neurol. 26, 41–46. 10.1002/ana.410260106. [PubMed: 2549845]

Highlights

- Glutamatergic neurons of the PPN and CnF show distinct biophysical differences
- CnF neurons produce bilateral muscle activation and involuntary locomotor activity
- PPN neurons elicit long-lasting muscle activity and decreased overall motor output

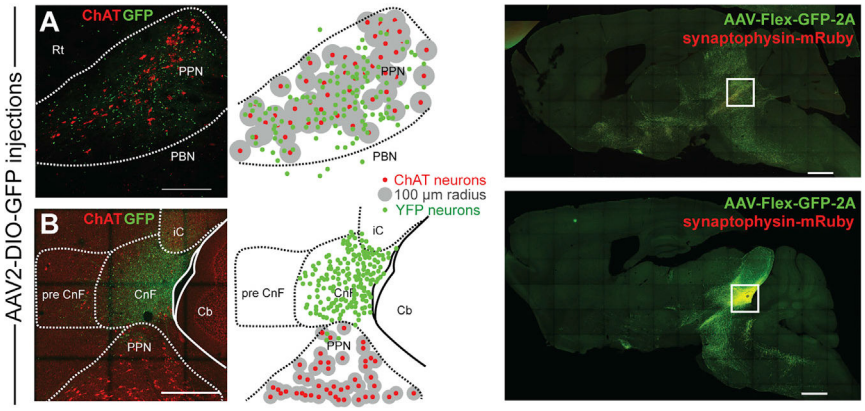

Figure 1. Segregation of MLR structures by viral transduction

(A and B) Viral injection volume was adjusted to be restricted within the border of the PPN (A) or the CnF (B) using as a marker the expression of choline acetyltransferase (ChAT; 100-µm radius, sagittal plane). The dorsal and ventral borders of the PPN were defined as a 100-µm distance from the outer cholinergic neuron soma (A), whereas the ventral border of the CnF was 100 µm farther from cholinergic neurons (B). Low magnification of the injection site for the PPN and CnF (right).

Scale bars: (A) 250 µm, (B) 500 µm, (right panels) 1,000 µm.

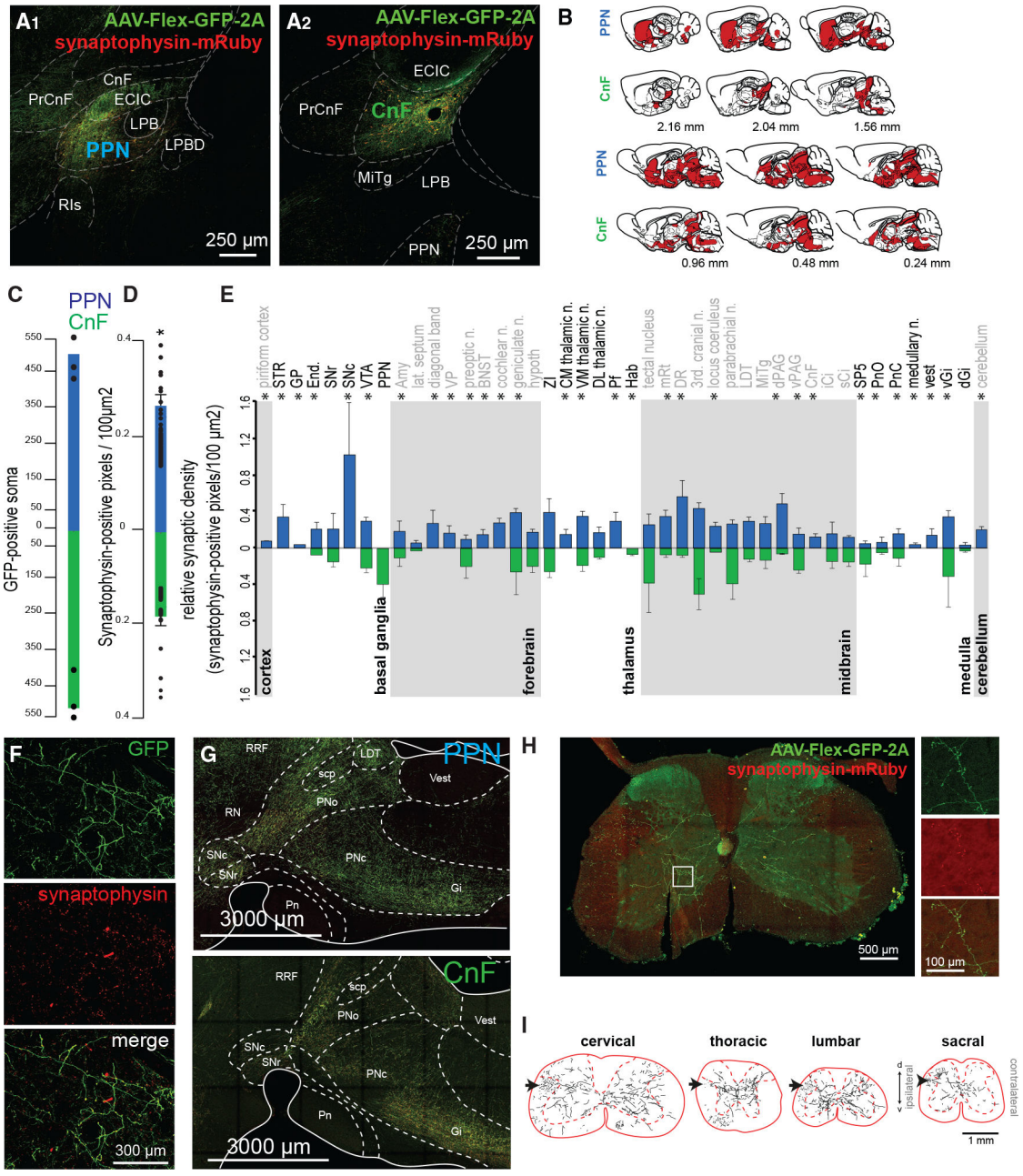

Figure 2. Axonal distribution of PPN and CnF glutamatergic neurons

(A and B) Following injection of AAV-DIO-GFP-2A-synaptophysin-mRuby limited to the PPN (A1) or the CnF (A2) borders based primarily on ChAT staining (A1′ and A2′), we observed widespread distribution of GFP-labeled axons across the brain (sagittal plane) (B). (C and D) Quantification of the total count of GFP-positive soma (PPN: 504.66 ± 58.42, CnF: 518.33 ± 54.67; one-way ANOVA, $F_{(1,5)} = 0.03$, $p = 0.87$) and overall synaptic density (PPN: 0.27 ± 0.024 pixels/100 µm^2, CnF: 0.18 ± 0.02 pixels/100 µm^2; one-way ANOVA, $F_{(1,86)} = 7.64$, $p = 0.007$).

(E) Segregated synaptophysin labeling across the brain revealed distinct patterns of innervation by PPN and CnF glutamatergic neurons, particularly in the basal ganglia, forebrain, thalamus, midbrain, medulla, and cerebellum (Wilcoxon test).
(F) Fluorescent micrographs illustrating a representative example of GFP and synaptophysin labeling in the striatum following PPN transduction.
(G) Distribution of axons in the brainstem following PPN and CnF injections (sagittal plane).
(H) Synaptic distribution in a cervical segment of the spinal cord.
(I) Axonal reconstructions in typical examples of cervical, thoracic, lumbar, and sacral spinal cord segments following unilateral PPN injection. Black arrows represent the rubrospinal tract.
*$p < 0.05$. All experiments have been replicated in at least 3 mice. A single datum is represented by a small dot. All data are represented as mean ± SEM. Scale bars: (A) 250 μm, (A′) 50 μm, (F) 300 μm, (G) 3,000 μm, (H) 500 μm, (H, inset) 100 μm, (I) 1 mm.

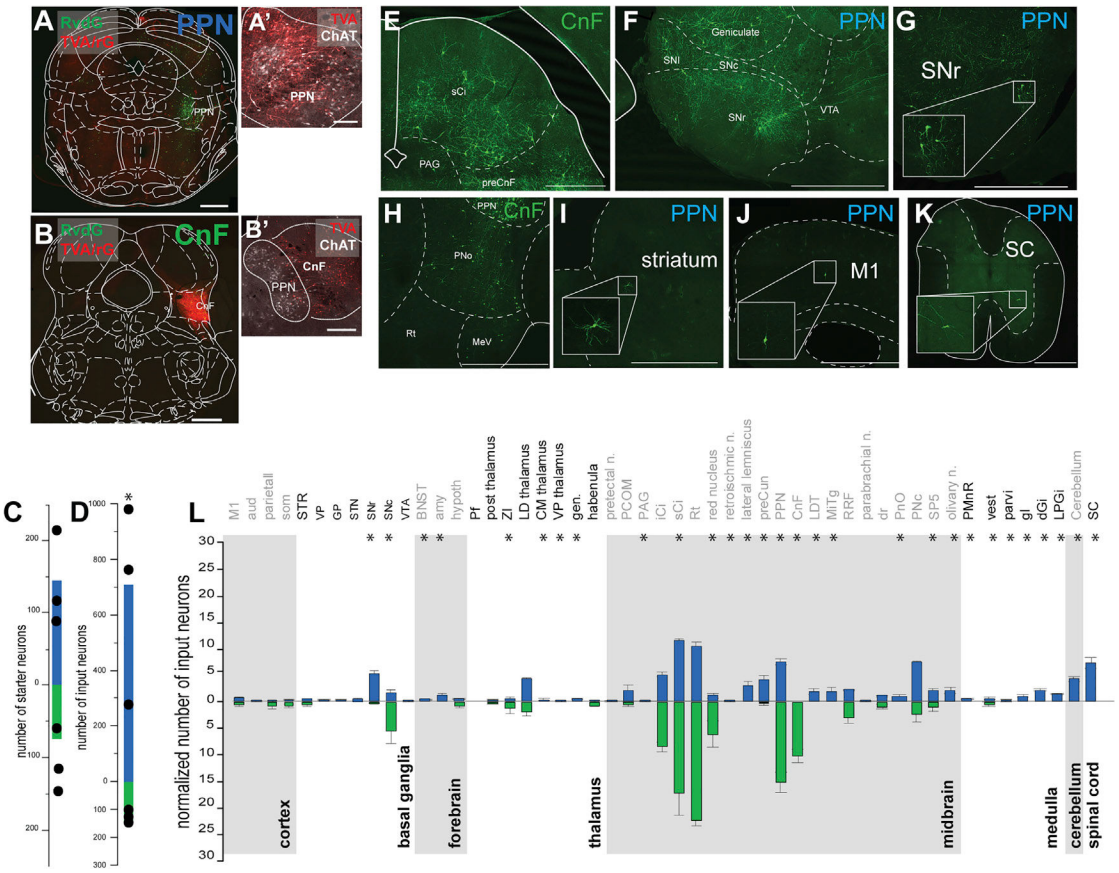

Figure 3. Whole-brain inputs to PPN and CnF glutamatergic neurons

(A–D) Following injection of helpers (mCherry, red) and rabies virus (YFP, green) in the PPN (A) and the CnF (B) defined using ChAT staining (A′ and B′), we quantified the number of starter neurons (PPN: 145.33 ± 40.19, CnF: 74.66 ± 24.91; t test: $t_{(4)} = 1.49$, $p = 0.21047$) (C) and the number of input neurons across all brain areas (raw: PPN: 708.91 ± 242.25, CnF: 143.33 ± 12.17, t test: $t_{(4)} = 2.33$, $p = 0.0401$; normalized: PPN: 4.73 ± 1.27, CnF: 2.28 ± 0.94 input/starter, Mann-Whitney: $Z = 1.964$, $p = 0.0495$) (D). Due to the higher number of RvdG-labeled neurons following injection in the PPN compared with the CnF, the signal intensity was focused on the YFP signal for the PPN and the mCherry signal for the CnF (coronal plane).

(E–K) Fluorescent micrographs of representative areas where input neurons were identified, including the dorsal brainstem (E) and the pons (H) following a CnF injection and the ventral midbrain (F and G), the striatum (I), the cortex (J), and the spinal cord (K) following a PPN injection.

(L) Quantification of the number of input neurons projecting to PPN (blue) and CnF (green) glutamatergic neurons for each brain area normalized by the overall total number of input neurons per animal (Wilcoxon test).

*$p < 0.05$. All experiments have been replicated in at least 3 mice. A single datum is represented by a small dot. All data are represented as mean ± SEM. Scale bars: (A and B) 500 μm, (A′) 100 μm, (B′) 250 μm, (E–K) 1,000 μm.

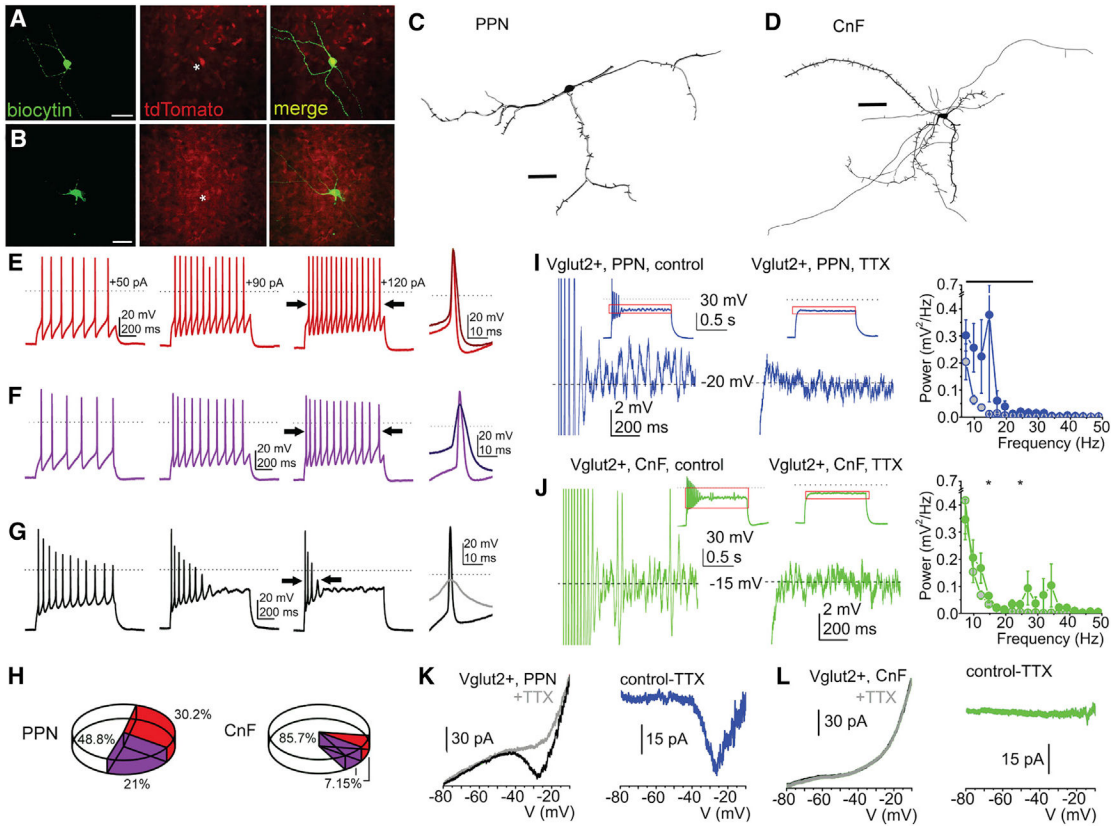

Figure 4. Functional and morphological differences of PPN and CnF glutamatergic neurons

(A and B) Fluorescent micrographs of PPN and CnF glutamatergic neurons obtained from VGLUT2-tdTomato mice following biocytin labeling.

(C and D) Reconstruction of representative glutamatergic neurons in the PPN (C) and the CnF (D) in the coronal plane, which were subsequently used to quantify the number of proximal dendrites, nodes, and endings (Table S2).

(E–G) Changes of spike frequency adaptation by increasing depolarizing steps revealed functional subtypes of glutamatergic neurons defined as follows: (E) non-adapting, or less than 50% increase in the adaptation index of the action potential trains obtained with 50 and 120 pA current injections; (F) slowly adapting, or more than 50% change of the adaptation index but fired during the whole 1 s-long depolarizing step; and (G) rapidly adapting, or paused firing after application of greater depolarizing steps.

(H) Proportion of neurons with different spike frequency adaptation properties in the PPN and the CnF.

(I and J) Voltage traces from glutamatergic neurons in the PPN (I) and the CnF

(J) representing high-threshold oscillations during 120 pA depolarizing square current injections under control conditions (left) and following TTX application (right; red squares of the small inserts indicate the magnified area). Related power spectra are displayed on the left (average ± SEM; PPN control, black circles; PPN+TTX, gray circles with black contours; CnF control, red circles; CnF+TTX, gray circles with red contours).

(K and L) Representative current traces from neurons in the PPN (K) and the CnF (L) elicited by voltage ramp injections under control conditions (black) and with TTX (gray; left). TTX-sensitive currents are shown in the right panels (PPN, blue; CnF, green). *$p < 0.05$. All experiments have been replicated in at least 3 mice. Group value and statistics are provided in Table S2. All data are represented as mean ± SEM. Scale bars: (A and B) 0.5 mm, (C and D) 50 μm.

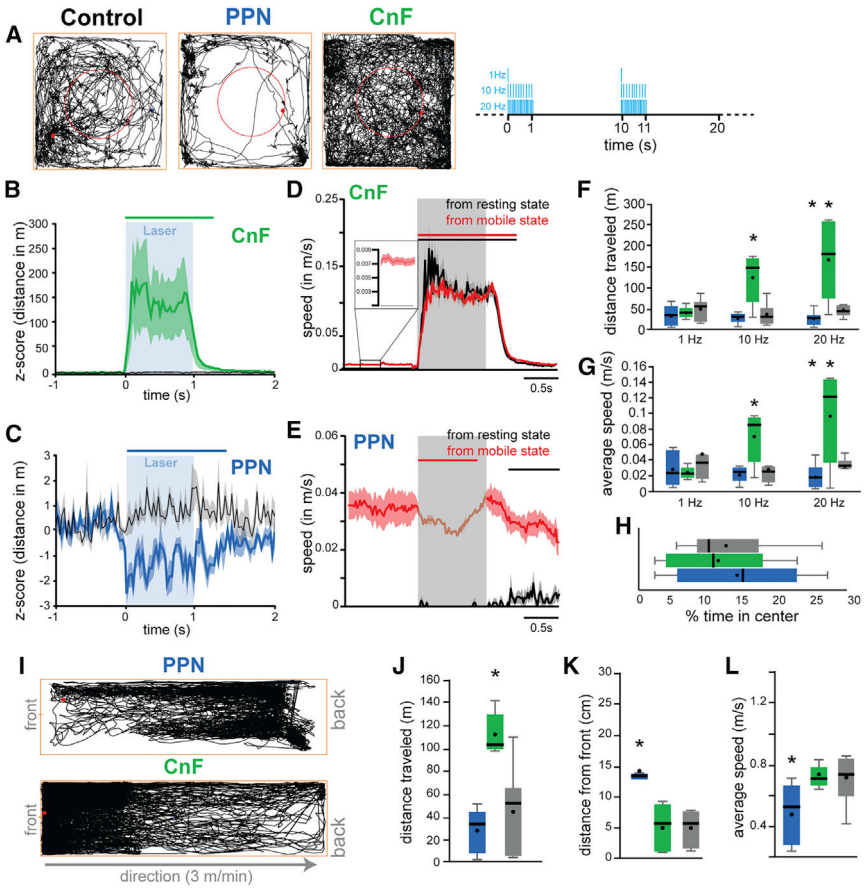

Figure 5. Locomotor effects following stimulation of PPN and CnF glutamatergic neurons

(A) Trace examples of control-, PPN-, and CnF-stimulated animals tested in the open field. The red circle represents the center of the arena. Right, stimulation protocol used for each frequency (1–20 Hz, 20-ms pulses, 1 s on/9 s off). The behavior was recorded at a resolution of 120 frames per second.

(B and C) Normalized distance traveled during individual 10-Hz stimulation of CnF (B) or PPN (C) glutamatergic neurons; control animals (gray; wild type) received the same experimental treatment (two-way multivariate analysis of variance [MANOVA] groups × stimulation: group effect, $F_{(2,491)} = 198.21$, $p = 0.00001$; stimulation effect, $F_{(2,491)} = 503.43$, $p = 0.00001$; interaction effect, $F_{(4,491)} = 201.55$, $p = 0.00001$; post hoc Bonferroni, $P_{CNFstim\_PPNstim} = 0.0001$, $P_{CNFstim\_CTRLstim} = 0.0001$, $P_{PPNstim\_CTRLstim} = 0.0001$). The line above represents the statistical difference of the distance traveled compared with the baseline (1 s).

(D and E) Distance traveled during individual stimulation of CnF (D) or PPN (E) glutamatergic neurons during resting (black) or during spontaneous movement (activity during baseline: PPN, 0.0195 cm/s; CnF, 0.0492 cm/s; 3-way mixed ANOVA structure × state × stimulation: stimulation effect, $F_{(2,443)} = 9$, $p = 0.0001$; structure, $F_{(1,443)} = 79.95$, $p = 0.00001$; state, $F_{(1,443)} = 2792.70$, $p = 0.00001$; interaction, $F_{(4,443)} = 30.72$, $p = 0.00001$; post hoc Bonferroni: $P_{PPN\_mobile\_immobile} = 0.0001$, $P_{CNF\_mobile\_immobile} > 0.05$). The line above represents the statistical difference of the distance traveled compared with the baseline

(1 s). Insert in (D) shows a magnification of the baseline. Scales were adjusted based on the response and therefore differ between groups.

(F and G) Total distance traveled and average speed (in meters per second) during the 30-min session following stimulation at 1, 10, or 20 Hz (20-ms pulse) (distance traveled: two-way repeated measures ANOVA: $F_{group(2,62)} = 0.86$, $p = 0.433$, $F_{frequency(2,62)} = 5.22$, $p = 0.0102$, $F_{interaction(4,62)} = 6.83$, $p = 0.0003$; post hoc: 1 Hz: $P_{ctrl\text{-}CNF} = 0.256$, $P_{ctrl\text{-}PPN} = 0.11$; 10 Hz: $P_{ctrl\text{-}CNF} = 0.002$, $P_{ctrl\text{-}PPN} = 0.25$; 20 Hz: $P_{ctrl\text{-}CNF} = 0.002$, $P_{ctrl\text{-}PPN} = 0.035$; average speed: $F_{group(2,62)} = 2.71$, $p = 0.1046$, $F_{frequency(2,62)} = 1.93$, $p = 0.16$, $F_{interaction(4,62)} = 5.55$, $p = 0.0014$; post hoc: 1 Hz: $P_{ctrl\text{-}CNF} = 0.11$, $P_{ctrl\text{-}PPN} = 0.14$; 10 Hz: $P_{ctrl\text{-}CNF} = 0.008$, $P_{ctrl\text{-}PPN} = 0.25$; 20 Hz: $P_{ctrl\text{-}CNF} = 0.007$, $P_{ctrl\text{-}PPN} = 0.031$).

(H) Percentage of time spent in the center of the arena ($F_{(2,20)} = 0.30$, $p = 0.7426$).

(I) Representative traces of PPN- and CnF-stimulated animals on the constant-speed treadmill.

(J–L) Distance traveled, average distance from the front of the treadmill, and average speed following stimulation at 10 Hz (distance traveled: one-way ANOVA: $F_{(2,21)} = 24.03$, $p = 0.00001$; Bonferroni: $P_{PPN\_CTRL} = 1.0$, $P_{CTRL\_CNF} = 0.0001$, $P_{PPN\_CNF} = 0.0001$; distance to the front: $F_{(2,21)} = 14.44$, $p = 0.0001$; Bonferroni: $P_{PPN\_CTRL} = 0.0001$, $P_{CTRL\_CNF} = 0.715$, $P_{PPN\_CNF} = 0.001$; average speed: $F_{(2,21)} = 17.41$, $p = 0.0001$; Bonferroni: $P_{PPN\_CTRL} = 0.714$, $P_{CTRL\_CNF} = 0.0001$, $P_{PPN\_CNF} = 0.001$).

*$p < 0.05$. All experiments have been replicated in at least 3 mice. Whisker plots represent mean, median, standard error, and 25/75th percentile. All data are represented as mean ± SEM.

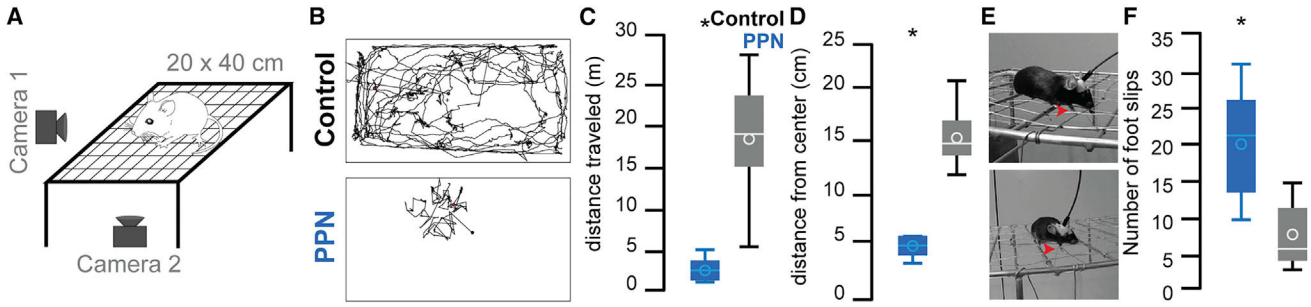

Figure 6. Modulation of gait by PPN glutamatergic neurons

(A) Representation of the elevated grid walk test.

(B) Representative traces in control and PPN groups (the CnF group is not shown, see the text for details) (stimulation parameters: 10 Hz, 20-ms pulses, 1 s on/9 s off).

(C and D) Distance traveled (two-tailed t test: $t_{(28)} = 7.8146$, $p = 0.00001$) and average distance to the center ($t_{(28)} = 6.34$, $p = 0.00001$) following 10-Hz stimulation.

(E) Representative images of mice making foot slips during the elevated grid-walk test.

(F) Total number of foot slips ($t_{(15)} = 5.29$, $p = 0.00001$).

*$p < 0.05$. All experiments have been replicated in at least 3 mice. Whisker plots represent mean, average, standard error, and 25/75th percentile.

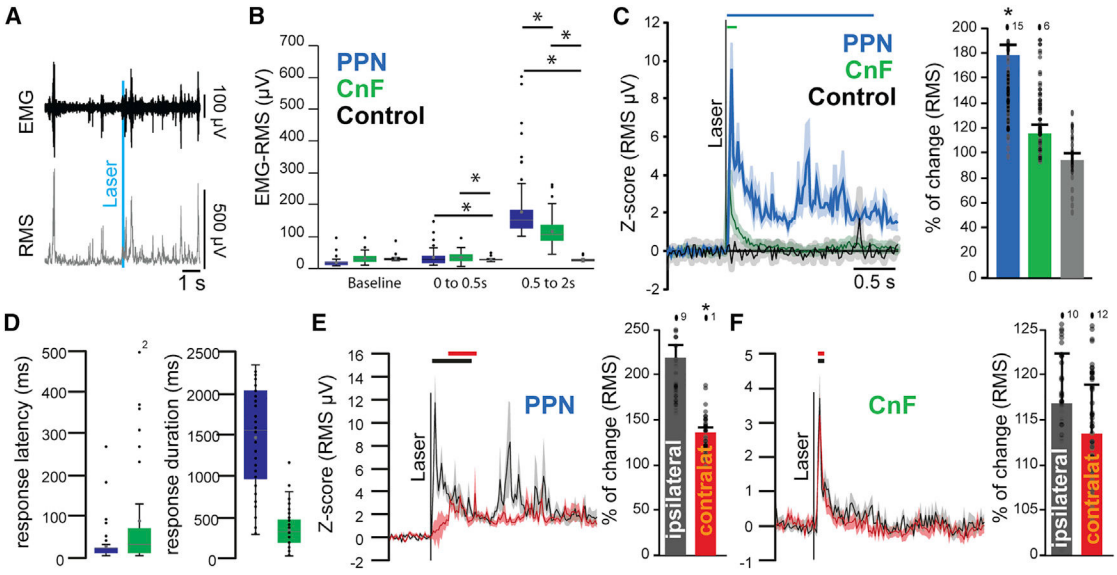

Figure 7. Differential involvement of PPN and CnF glutamatergic neurons in muscle tone generation

(A) Example of electromyogram (EMG) activity recorded at the level of the biceps following laser stimulation (10 Hz, 20-ms pulses, 1 s on/9 s off) and the conversion into root-mean-square (RMS).

(B) Raw amplitude (in microvolts) of the RMS-EMG of ipsilateral forelimb biceps during baseline or immediately or 500 ms after single-stimulation pulses delivered in the PPN, CnF, or sham (0–0.5 s after stimulation: one-way ANOVA: $F_{(2,214)} = 5.59$, $p = 0.0001$; post hoc Bonferroni: $P_{PPN\_vs\_CTRL} = 0.004$, $P_{CNF\_vs\_CTRL} = 0.004$, $P_{PPN\_vs\_CNF} = 1.0$; 0.5 to 2 s after stimulation: $F_{(2,214)} = 46.62$, $p = 0.00001$; post hoc Bonferroni: $P_{PPN\_vs\_CTRL} = 0.0001$, $P_{CNF\_vs\_CTRL} = 0.0001$, $P_{PPN\_vs\_CNF} = 0.001$).

(C) Change in the RMS signal following repeated single-stimulation pulses recorded at the level of the biceps (percentage of change relative to the 1 s baseline: PPN: 178.60% ± 10.06%, CNF: 115.72% ± 3.93%, CTRL: 94.33% ± 4.55%; one-way ANOVA: $F_{(2,214)} = 26.26$, $p = 0.00001$; post hoc Bonferroni: $P_{PPN\text{-}CNF} = 0.0001$, $P_{PPN\text{-}CTRL} = 0.0001$, $P_{CNF\text{-}CTRL} = 0.804$).

(D) Response latency and duration of the significant increase in the RMS signal in response to PPN or CnF stimulation (latency: $F_{(1,212)} = 6.44$, $p = 0.019$; duration: $F_{(1,212)} = 19.29$, $p = 0.00001$).

(E and F) Change in the RMS signal in the ipsilateral and contralateral forelimbs biceps following stimulation in PPN groups (PPN_{ispi} = 218.08% ± 17.02%, PPN_{contra} 138.46% ± 5.71%; two-way ANOVA stim × side: $F_{stim(1,401)} = 648.221$, $p = 0.00001$, $F_{side(1,401)} = 39.6$, $p = 0.0001$, $F_{interaction} = 242.6$, $p = 0.00001$) and CnF groups (CnF_{ispi} = 117.06% ± 5.54%, CnF_{contra} = 113.55% ± 5.51%; two-way ANOVA stim × side: $F_{stim(1,401)} = 51.29$, $p = 0.00001$, $F_{side(1,401)} = 1.80$, $p = 0.18$, $F_{interaction(3,401)} = 18.30$, $p = 0.0000$). Lines represent the statistical difference compared with baseline.

*$p < 0.05$. All experiments have been replicated in at least 3 mice. Whisker plots represent mean, median, standard error, and 25/75th percentile; an individual datum is represented by

a small dot. Out-of-range data points are reported as numbers above the histogram. All data are represented as mean ± SEM.

KEY RESOURCES TABLE

REAGENT or RESOURCE	SOURCE	IDENTIFIER
Antibodies		
mCherry	ABCAM	(Abcam Cat# ab167453, RRID:AB_2571870)
ChAT	Merk Millipore	(Millipore Cat# AB144P, RRID:AB_2079751)
GFP	Thermofisher	(Thermo Fisher Scientific Cat# A-21311, RRID:AB_221477)
anti-Goat CY3	Jackson Immuno-research	(Jackson ImmunoResearch Labs Cat# 705-165-147, RRID:AB_2307351)
anti-Goat CY5	Jackson Immuno-research	(Jackson ImmunoResearch Labs Cat# 705-175-147, RRID:AB_2340415)
anti-mouse CY3	Jackson Immuno-research	(Jackson ImmunoResearch Labs Cat# 715-165-150, RRID:AB_2340813)
anti-rabbit 488	Jackson Immuno-research	(Jackson ImmunoResearch Labs Cat# 711-545-152, RRID:AB_2313584)
anti-rabbit AMCA	Jackson Immuno-research	(Jackson ImmunoResearch Labs Cat# 711-155-152, RRID:AB_2340602)
Bacterial and virus strains		
AAV2-DIO-EF1α-YFP	UNC Vector Core	VB2089
AAV2-DIO-EF1α-YFP-2A-synaptophysin-mRuby	Stanford Vector Core	N/A
AAV5-DIO-TVA-mCherry	UNC Vector Core	Vb2090
AAV8-DIO-RG	UNC Vector Core	38043
RvDG-YFP	Salk Institute	VB4652
AAV2-Flex-EF1a-ChR2	UNC Vector Core	N/A
Experimental models: Organisms/strains		
Mice: B6;129S6-Gt(ROSA)26Sortm9(CAG-tdTomato)Hze/J	Jackson	007905
Mice: Slc17a6tm2(cre)Lowl (also called VGLUT2-ires-Cre)	Jackson	028863
Mice: C57BL/6	Jackson	000664
Software and algorithms		
MATLAB	MathWorks	Version 2021a
FluoView software	Olympus	N/A
Fiji software	Open source	N/A
Photoshop	Adobe	Version 5
Clampfit	Molecular Devices	Version 10.0
Till Vision software	Till	version 4.0.1.3
NeuroLucida software	MBF Bioscience	N/A
Anymaze	Stoelting	N/A